

ISSN 1916-9639

APPLIED PHYSICS RESEARCH

**Vol. 1, No. 1
May 2009**



Canadian Center of Science and Education

Editorial Board

- Ajay K Pandey University of St Andrews, UK
- Anne Brown Canadian Center of Science and Education, Canada
- Christopher Andrew Hooley University of St Andrews, UK
- Hwee San Lim Universiti Sains Malaysia, Malaysia
- Igor Meglinski Cranfield University, UK
- Kaza Venkata Ramana Rao University of Rajasthan, India
- Khalid Omar Universiti sains Malaysia, Malaysia
- Makbul Anwari Universiti Teknologi Malaysia, Malaysia
- Mike Gibbs University of Sheffield, UK
- Nikolaus Klaus Metzger University of St Andrews, UK
- Patrick McNally Dublin City University, Ireland
- Paul Alan Hatherly Open University, UK
- Puramanathan Naidoo Mangosuthu University of Technology, South African
- Riccardo Bartolini University of Oxford, UK
- Stanislav Victorovich Shutov National Academy of Sciences of Ukraine, Ukraine
- Stephen Daniels Dublin City University, Ireland
- Yevgen Baganov Kherson National Technical University, Ukraine



Contents

The Effect of DC Plating Parameters on the Composition and Morphology of Silver-copper Alloy	2
<i>C.Shanthi, S.Barathan, RajasrisenJaiswal & R.M. Arunachalam</i>	
Electrospinning Fabrication of Polycrystalline LaCrO ₃ Porous Hollow Nanofibers	8
<i>Jinxian Wang, Xiangting Dong, Qizheng Cui, Guixia Liu & Wensheng Yu</i>	
Mapping of Individual Oil Palm Trees Using Airborne Hyperspectral Sensing: An Overview	15
<i>Kamaruzaman Jusoff & Mubeena Pathan</i>	
Study on the Optimization Method of Transducer Linear Transmission Function Based on Structural Parameter Adjustment	31
<i>Guangxu Lin</i>	
Effect of Nickel on the Structural Properties of Mn Zn Ferrite Nano Particles	41
<i>C.Venkataraju</i>	
On the Independence of KVL	46
<i>Zaiqi Fu & Wenliang Wu</i>	



The Effect of DC Plating Parameters on the Composition and Morphology of Silver-copper Alloy

C. Shanthi (Corresponding author)

Department of Physics

Sona College of Technology

Salem 636005, Tamilnadu, India

Tel: 91-427-409-9791 E-mail: shanthi_rec@yahoo.co.in

S. Barathan

Department of Physics

Annamalai University

Annamalai nagar-608002, Tamilnadu, India

Tel: 91-414-422-2751 E-mail: sbarathan_au@rediffmail.com

Rajasrisen Jaiswal

Department of Physics

Sona College of Technology

Salem-636005, Tamilnadu, India

Tel: 91-427-409-9823 E-mail: senoritta_in@yahoo.co.in

R.M. Arunachalam

Department of Mechanical Engineering,

Sona College of Technology

Salem-636005, Tamilnadu, India

Tel: 91-427-409-9716 E-mail: arun_rm@yahoo.com

The research is financed by All India Council for Technical Education (AICTE), New Delhi under the Research Promotion Scheme File No. 8023/BOR/RPS-145 /2006-07 and Sona College of Technology.

Abstract

This research attempts to optimize the parameters for DC plating of silver on silver alloy of two different compositions namely 50% and 75% silver alloy. In the Silver-copper alloy, the surface morphology and composition of the electro deposit are influenced by current density, silver concentration in the bath, applied current type and addition of additive. It has been found that concentration of silver in silver alloy has an effect in weight

electrodeposited over cathode in DC plating. The surface morphology is studied by taking SEM micrograph for the two different compositions of silver alloy and grain size is measured using XRD analysis. Higher the purity of silver, finer is the grain size. It has been observed that with the increase of silver in the sample, the amount of silver deposited, hence the thickness of the deposit varies for the same current and voltage settings.

Keywords: DC plating, Silver alloy, Current density, Thickness

1. Introduction

Electroplated silver was developed primarily for use on hollowware, flatware and tableware. It has proven its usefulness in both decorative and functional applications in both Engineering, electrical and electronic applications. Its great success has been virtually a complete replacement of gold on metallic lead frames, the devices that support majority of silicon chips. Silver has been used as a bearing surface for many decades. Silver is plated almost exclusively with cyanide based solutions, despite the considerable research effort that has been expended on evaluating less toxic alternatives. It is possible to produce fully bright deposits that require no further buffing or polishing. This is achieved by including a brightening agent in the solution formula (Sarkar, 1971). Silver holds a distinguished position among the metals as it was the first metal covered by a patent for electroplating (Orr, 1982). Copper is the only metal with which silver forms a simple eutectic between two well defined terminal solid solutions. The salient feature of this system is that useful alloys are found over the full range of composition. The fact that the eutectic is between two terminal solid solutions, each having very similar properties, is largely responsible for this. The silver copper eutectic is the basis for the large family of silver –copper-zinc and silver copper zinc cadmium industrial brazing alloys. This alloy has the best combination of strength, hardness and electrical properties of any of the silver alloys. Numerous silver copper alloys in the range 99.8 percent silver down to 50 percent have been used for electric contacts, brazing and silver jewellery industry (McDonald, 1982). This research attempts to optimize the parameters for DC plating of silver over silver alloy for two different compositions namely 75% silver, 25% copper and 50% silver and 50% copper. DC plating is the process of depositing a coating having a desirable form by means of electrolysis. The main purpose is to alter the characteristics of a surface so as to provide improved appearance, ability to withstand corrosive agents, resistance to abrasion or other desired properties or a combination of them (Nasser Kanani, 2004). But with the advent of pulse plating, which is defined as metal deposition by pulsed electrolysis (interrupted direct current to electroplate parts) the above said properties are improved (Knodler, A., 1986). Pulse plating leads to smoother and fine grained deposits (Shanthi, et al., 2008) and almost completely free of pinholes. Pulse plating also reduces the variation of plating thickness from one part to the next. Plating speeds can be increased. Current efficiency is improved and raw material consumption is also low. Our present investigation is to optimize the parameters for DC plating of silver on silver alloy of two different compositions namely 50% and 75% silver alloy.

2. Experimental

2.1 Bath composition

Potassium cyanide, Silver Potassium cyanide and Commercial Brightener are the main composition of the bath with a silver content of 30gms/litre (Canning, W., 2005). The purity of the anode silver is 99.99%. Anode and cathode size ratio should be 2:1. Silver metal concentration is normally maintained by anode dissolution which needs small additions of metal salt occasionally. This is processed further by adding either silver cyanide or potassium silver cyanide. Silver is present as potassium silver cyanide, and its concentration must be maintained by making periodic additions of this double salt. Buffer salt is added to maintain the pH level.

2.2 Specimen Preparation

Samples from two different silver compositions namely 50% and 75% silver alloy are prepared by melting 50grams of pure silver and 50grams of copper and 75grams of pure silver and 25grams of copper at a temperature of 1100°C in a crucible using a charcoal furnace respectively. The molten silver ingot is poured in a rectangular casting plate of length 3cm and height 0.7cm and cooled at room temperature. This ingot is pressed and rolled in a press roller to get 0.17cm thickness sheet. Then it is cut into a size of 7cmX 2.5cm. Surface of the specimen was cleaned with acid pickling and polished in a vibrator polisher and finally hand brushed and cleaned with tap water.

2.3 Procedure of conducting the experiment

The anode which is annealed pure silver (99.99%) is connected to the positive terminal of the rectifier and the specimen cathode is connected to the negative terminal of the rectifier. A filter unit is used to remove the impurities in bath continuously. Deposition of silver is on the cathode silver alloy which undergoes a displacement of 8.75cm/second to avoid polarization in the solution. DC plating is studied for the peak current densities of 3.2103A/dm², 3.7453A/dm² and 4.5479A/dm² by giving a value to ON time and making the OFF time zero in the pulse rectifier. A DC voltage of 1.2volt and DC current of 1.2, 1.4 and 1.7 amp are set up and plating is done for 60 seconds with suitable bath composition. The cathode is weighed before and after electroplating and theoretical, experimental thickness, current efficiency are calculated and hardness measured using microhardness tester are recorded as shown in the Table 1.

3. Results and discussion

Samples from two different silver compositions namely 50% and 75% silver alloy have been made and electrodeposited. Figure 1 shows the SEM micrograph for DC plating of 75%silver and 25% copper alloy for a peak current density of 3.7453A/dm² and figure 2 shows the SEM micrograph for DC plating of 50% Silver and 50% Copper alloy for the same peak current density of 3.7453A/dm². In the Silver –copper alloy, the surface morphology and composition of the electro deposit are influenced by current density, silver concentration in the bath, applied current type and addition of additive (Mohan, et al.,2005).The increase of current density has increased the amount of weight electrodeposited and hence the thickness of the silver deposit. Experimentally it is determined that the current density for minimum time and maximum deposition as 3.7453A/dm² for 50% silver alloy and 4.5479A/dm² for 75% silver alloy for a specimen size of 0.7dm x 0.25dm beyond which darkening of the specimen is observed. Burning deposit is found in 50% silver alloy for a peak current density of 4.5479A/dm² and the hardness is found to be maximum. The current efficiency is found to be maximum for a current density of 3.7453A/dm² for 50% silver alloy and 75% silver alloy. It is found that concentration of silver in silver alloy has an effect in the weight electrodeposited over cathode in DC plating. Pure silver has low resistance, high current flow and so conductivity is more. It has been observed that with the increase of silver in the sample, the amount of silver deposited, hence the thickness of the deposit varies for the same current and voltage settings. Hence more amount of silver has been electrodeposited for 50% silver compared to 75% silver. But for 50% silver, at a current density of 4.5479amp/dm², the current efficiency decreases to a large extent due to the formation of burnt deposit on the specimen and the hardness also increased. The deposits are not smooth and it is coarse grained in DC plating. Plating thickness varies from one part to the next. Plating speed is less and current efficiency is also less. Raw material consumption is high (Shanthi, et al., 2007).

3.1 Grain size measurement using XRD

Figure 3 shows the XRD pattern for 75% Silver and 25% Copper and Figure 4 shows the XRD pattern for 50% Silver and 50% Copper. The grain size is calculated using Debye Scherer equation. It is observed that the grain size is finer for 75% Silver than that for 50% silver. The concentration of silver in silver alloy plays a vital role in determining the grain size. Higher the purity of silver, finer is the grain size.

4. Conclusion

Based on the conducted studies on DC plating of silver on silver alloy of two different compositions namely 75% silver, 25% copper and 50% silver, 50% copper, it has been found that the concentration of silver in the cathode plays a role in deciding the amount of silver deposited on the cathode. It has been observed that with the increase of silver in the sample, the amount of silver deposited, hence the thickness of the deposit varies for the same current and voltage settings. Higher the purity of silver, finer will be the grain size. Current density above 3.7453A/dm² for 50% silver alloy and 4.5479A/dm² for 75% silver alloy leads to darkening of the deposits. The 75% silver alloy can withstand more current density than 50% silver alloy. For 50% silver, at a current density of 4.5479amp/dm², the current efficiency decreases to a large extent due to the formation of burnt deposit on the specimen and the hardness also increased. It is suggested that the properties are improved if the concentration of silver in silver copper alloy is more.

References

- Canning, W. (2005). *The Canning handbook surface finishing technology*. (23rd ed.). New Delhi: CBS publishers and distributors, (Chapter 19).
- Knodler, A. (1986). Pulsed electrodeposition of precious metals. In Jean-Claude, Puipe, & Frank Leaman (Eds.), *Theory and practice of pulse plating*. Florida: American electroplaters and surface finishers society, pp.164–174.
- McDonald, A.S., Price, B.R. & Sistare, G.H. (1982). Alloying behavior of silver and its principal binary alloys. In Allison Butts, & Charles D. Coxe (Eds.), *Silver economics, metallurgy and use*. Florida: Robert Krieger Publishing Company, pp.248-254.
- Mohan, S., & Raj, V. (2005). The effect of additives on the pulsed electrodeposition of copper. *Transactions of Institute of metal finishing*, 83,194-198.
- Nasser Kanani, (2004). *Electroplating-Basic Principles: Processes and practice*. Berlin, Germany: Elsevier Ltd, (Chapter 4).
- Orr, M.A. (1982). Electroplating. In Allison Butts, Charles D. Coxe (Eds.), *Silver economics, metallurgy and use* (pp.180-189). Florida: Robert Krieger Publishing Company.
- Sarkar, S. (1971). *Silver the Science and Technology*. Calcutta: Calcutta Book house, (Chapter 4).
- Shanthi, C., Arunachalam, R.M., & Barathan S. (2007). *Study of Surface Morphology in DC plating of Silver for the Jewellery Industry*, paper presented at National Conference on Advances in Surface and Interface Analysis, Salem, India.
- Shanthi, C., Barathan, S., RajarisenJaiswal, Arunachalam, R.M., & Mohan, S. (2008). The effect of pulse parameters in electrodeposition of silver alloy. *Materials letters*, 62, 4519–4521.

Table 1. DC plating parameters for 75% and 50% silver alloy.

% of Silver	DC Current Ampere	Current density A/dm ²	Theoretical weight grams	Theoretical Thickness micrometer	Experimental Thickness micrometer	Weight Electrodeposited grams	Current Efficiency %	Hardness VPN
75%	1.2	3.2103	0.0805	2.1427	1.7302	0.065	80.75	80.3
	1.4	3.7453	0.0939	2.4995	2.1828	0.082	87.33	82.4
	1.7	4.5479	0.114	3.0355	2.5821	0.097	85.09	86.7
50%	1.2	3.2103	0.0805	2.2323	2.0243	0.073	90.68	88.3
	1.4	3.7453	0.0939	2.6039	2.5234	0.091	96.91	81.7
	1.7	4.5479	0.114	3.1612	2.5511	0.092	80.70	102

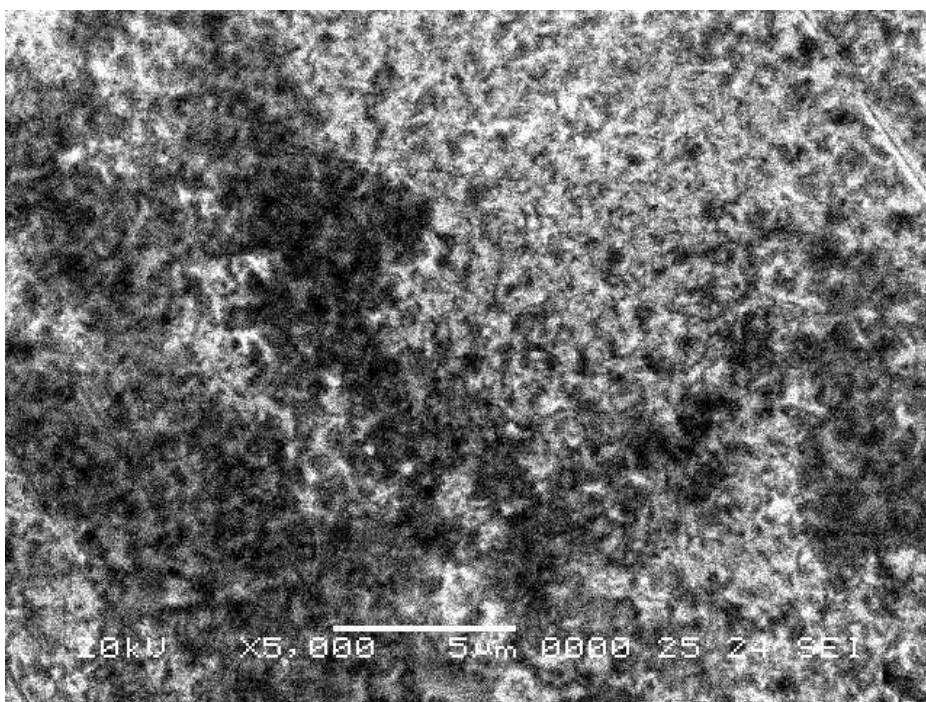


Figure 1. SEM micrograph for DC plating of 75%silver and 25% copper alloy for a peak current density of $3.7453\text{A}/\text{dm}^2$

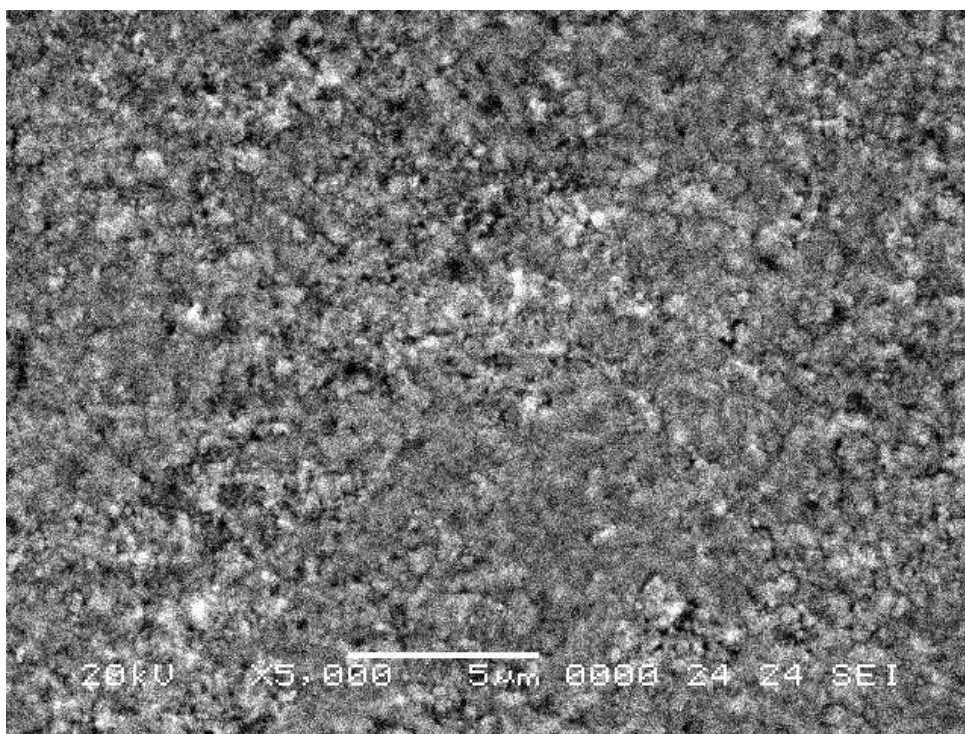


Figure 2. SEM micrograph for DC plating of 50% Silver and 50% Copper alloy for a peak current density of $3.7453\text{A}/\text{dm}^2$

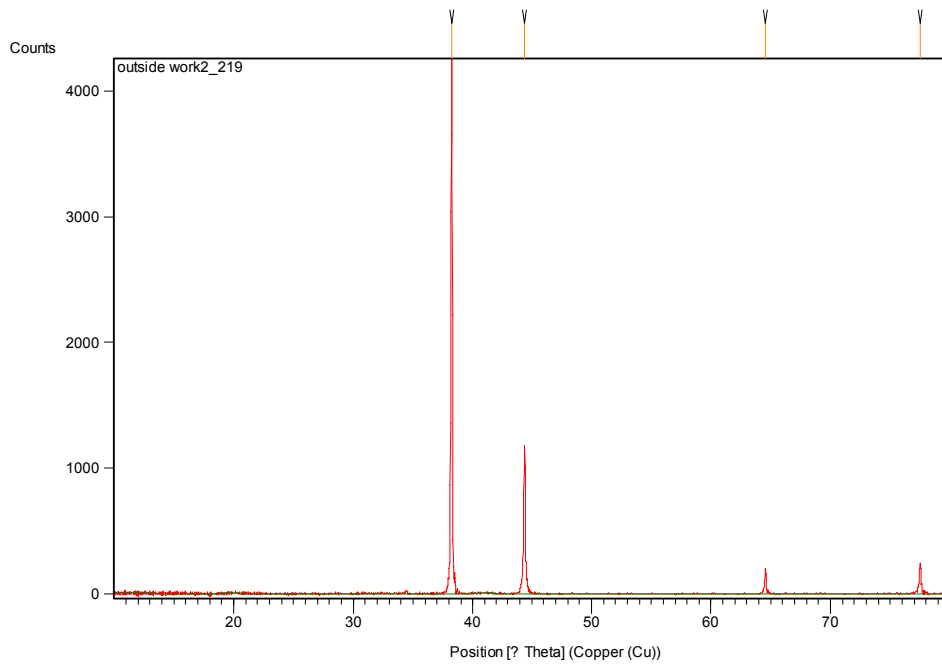


Figure 3. XRD pattern for 75% Silver and 25% Copper alloy for a peak current density of 3.7453A/dm²

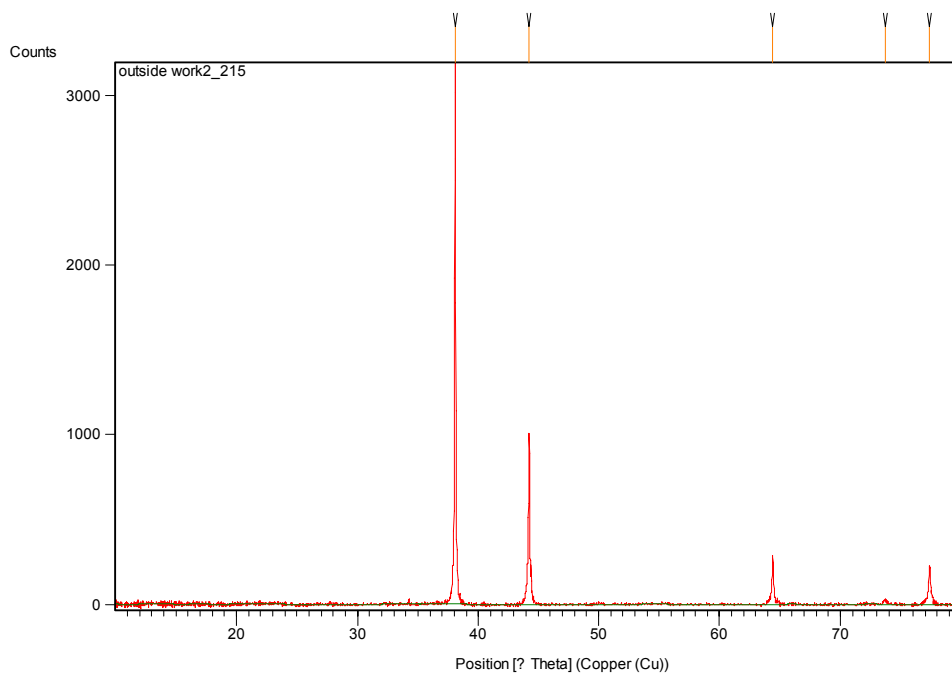


Figure 4. XRD pattern for 50% Silver and 50% Copper alloy for a peak current density of 3.7453A/dm²



Electrospinning Fabrication of Polycrystalline LaCrO₃ Porous Hollow Nanofibers

Jinxian Wang, Xiangting Dong (Corresponding author) & Qizheng Cui

School of Chemistry and Environmental Engineering

Changchun University of Science and Technology

Jilin 130022, China

Tel: 86-431-8558-2574 E-mail: dongxiangting888@yahoo.com.cn

Guixia Liu & Wensheng Yu

School of Chemistry and Environmental Engineering

Changchun University of Science and Technology

Jilin 130022, China

This work was financially supported by the Science and Technology Development Planning Project of Jilin Province (Grant Nos. 20040125, 20060504, 20070402), the Scientific Research Planning Project of the Education Department of Jilin Province (Under grant Nos. 200224, 2005109, 2007-45)

Abstract

Polyvinyl Pyrrolidone(PVP)/[La(NO₃)₃+Cr(NO₃)₃] composite nanofibers were fabricated by electrospinning. SEM micrographs indicated that the surface of the prepared composite fibers was smooth, and the diameter of the nanofibers was in the range of 1-3 μ m. XRD analysis revealed that the composite nanofibers were amorphous in structure. LaCrO₃ nanofibers were fabricated by calcination of the PVP/[La(NO₃)₃+Cr(NO₃)₃] composite fibers. The diameters of LaCrO₃ nanofibers were smaller than those of the relevant composite fibers. The surface of the LaCrO₃ nanofibers became coarse with the increase of calcination temperatures. LaCrO₃ hollow-centered and porous nanofibers formed by nanoparticles were acquired when firing temperature was 600-900°C. SEM images indicated that the diameters of the synthesized LaCrO₃ nanofibers ranged from 500 to 800nm, and their lengths were greater than 100 μ m. XRD analysis revealed that LaCrO₃ nanofibers were orthorhombic in structure with space group Pbnm. Possible formation mechanism for LaCrO₃ nanofibers was preliminarily proposed.

Keywords: Electrospinning, Nanofibers, La, Cr, LaCrO₃

1. Introduction

The science and technology of nanostructured materials is advancing at a rapid pace (Mohapatra, 2008 & Zhang, 2007). Over the past decade, the preparation and functionalization of one-dimensional nanostructured materials has become one of the most highly energized research fields (Hu, 2008 & Kar, 2006). One-dimensional nanostructured materials, such as nanowires, nanorods, nanowhiskers and nanofibers, have stimulated great interests due to their importance in basic scientific research and potential technological applications (Huynh, 2002 & Duan, 2003). They are expected to play an important role as both interconnects and functional components in the fabrication of nanoscale

electronic and optoelectronic devices. In order to obtain these materials, various preparation methods have been developed including arc discharge, laser ablation, template, precursor thermal decomposition, and other methods (Iijima, 1991, Morales, 1998, Shi, 2001 & Pan, 2001). Electrospinning technique is widely applied to prepare polymers nanofibers (Li, 2004, 1151-1170). Recently, some inorganic compounds nanofibers have been prepared by electrospinning technique using electrospun fibers of polymer/inorganic composite as the precursor (Li, 2004, Zhang, 2008 & Shao, 2004). This processing involved the following three steps: (1) Preparation of a gel with suitable inorganic precursor and proper polymer, and achieving the right rheology for electrospinning process; (2) Electrospinning of the gel to obtain fibers of polymer/inorganic precursors composite; (3) Calcinations of the composite fibers to obtain final oxide fibers. It is important; however, to control all of the above three steps in order to obtain high quality fibers with the desired final properties. LaCrO_3 has attracted much interest recently due to their specific electrical and catalytic properties (Dong, 1994 & Yang, 2003). A few methods on the preparation of LaCrO_3 nanocrystalline materials were reported (Zhang, 2005 & Johnson, 2004). However, to the best of our knowledge, there have been no reports on the preparation of LaCrO_3 porous hollow nanofibers by electrospinning. In this paper, LaCrO_3 nanofibers were fabricated by calcination of the electrospun fibers of PVP/(lanthanum nitrate and chromium nitrate) composite, and some new results were obtained.

2. Experimental section

2.1 Chemicals

Polyvinyl pyrrolidone (PVP) ($M_r \approx 10000$) and chromium nitrate enneahydrate [$\text{Cr}(\text{NO}_3)_3 \cdot 9\text{H}_2\text{O}$] were purchased from Tianjin Kermel Chemical Reagents Development Center. Lanthanum nitrate hexahydrate [$\text{La}(\text{NO}_3)_3 \cdot 6\text{H}_2\text{O}$] was obtained from Tianjin Guangfu Institute of Fine Chemicals. All chemicals were analytically pure and directly used as received without further purification. Distilled water was used as solvent.

2.2 Preparation of PVP/[$\text{La}(\text{NO}_3)_3$ and $\text{Cr}(\text{NO}_3)_3$] composite gel

PVP/[$\text{La}(\text{NO}_3)_3$ and $\text{Cr}(\text{NO}_3)_3$] composite solution was prepared by dissolving 14.2568g of PVP powders, 2.3830g of $\text{La}(\text{NO}_3)_3 \cdot 6\text{H}_2\text{O}$ and 2.2021g of $\text{Cr}(\text{NO}_3)_3 \cdot 9\text{H}_2\text{O}$ in 12.15g of distilled water, and stirring for 10h, then remaining motionlessly for 2h. Thus, a viscous gel of PVP/[$\text{La}(\text{NO}_3)_3 + \text{Cr}(\text{NO}_3)_3$] composite containing 46%(wt%) PVP, 10%(wt%) metallic nitrate, 44%(wt%) H_2O , and the molar ratio 1:1 of La^{3+} to Cr^{3+} were obtained for electrospinning processing.

2.3 Fabrication of PVP/[$\text{La}(\text{NO}_3)_3$ and $\text{Cr}(\text{NO}_3)_3$] composite fibers and LaCrO_3 nanofibers

The setup used for electrospinning was indicated in Figure 1. The above composite gel of PVP, $\text{La}(\text{NO}_3)_3$, $\text{Cr}(\text{NO}_3)_3$ and H_2O mixture was contained in a plastic syringe with a stainless steel needle on its top. A copper wire connected to a DC high-voltage generator was placed in the gel, and the gel was kept in the syringe by adjusting the angle between syringe and the fixing bar. A grounded aluminum foil served as counter electrode and collector plate. A voltage of 18 kV was applied to the composite gel and a sprayed dense web of fibers was collected on the aluminum foil. The collected fibers were PVP/[$\text{La}(\text{NO}_3)_3 + \text{Cr}(\text{NO}_3)_3$] composite fibers. The prepared composite fibers were dried initially at 70°C for 12h under vacuum, and then calcined at a heating rate of 120°C/h and remained for 10h at 300°C, 600°C and 900°C, respectively. Thus, LaCrO_3 nanofibers were obtained when calcination temperature is 600-900°C.

2.4 Characterization methods

XRD analysis was performed with a Holland Philips Analytical PW1710 BASED X-ray diffractometer using $\text{Cu K}\alpha_1$ radiation, the working current and voltage were 30mA and 40kV, respectively. Scans were made from 10° to 80° at the scanning speed of 3°/min, and step was 0.05°. The morphology and size of the fibers were observed with a S-4200 scanning electron microscope made by Japanese Hitachi company. FTIR spectra of the samples were recorded on BRUKER Vertex 70 Fourier transform infrared spectrophotometer made by Germany Bruker company, and the specimen for the measurement was prepared by mixing the sample with KBr powders and then the mixture was pressed into pellets, the spectrum was acquired in a wave number range from 4000 cm^{-1} to 400 cm^{-1} with a resolution of 4 cm^{-1} .

3. Results and discussion

3.1 XRD patterns

In order to investigate the lowest crystallizing temperature and the variety of phases, the PVP/[La(NO₃)₃+Cr(NO₃)₃] composite fibers and samples obtained by calcining the composite fibers at different temperatures for 10h were characterized by XRD, as indicated in Figure 2. The results showed that the PVP/[La(NO₃)₃+Cr(NO₃)₃] composite fibers were amorphous in structure, only a broad peak was located around 22°, it was the typical peak of the amorphous polymer, indicating that the composite fibers were amorphous in structure(Figure 2a). The sample was also amorphous at 300°C, and no obvious diffraction peaks could be observed(Figure 2b). The polycrystalline LaCrO₃ nanofibers with single phase were synthesized when calcination temperature was in the range of 600-900°C(Figure 2c and 2d), the d(spacing between crystallographic plane)values and relative intensities of LaCrO₃ are consistent with those of JCPDS standard card(24-1016), and the crystal structure of the prepared LaCrO₃ was orthorhombic system with space group Pbnm.

3.2 SEM images

In order to study the morphology and size of the as-synthesized fibers, the prepared fibers were investigated by SEM, as shown in Figure 3. As seen from Figure 3, the morphology and size of the fibers varied strongly with the increase of calcination temperatures. The surface of the PVP/[La(NO₃)₃+Cr(NO₃)₃] composite fibers was very smooth, and the diameter of the composite fibers was in the range of 1-3μm. The morphology and size of the fibers at 300°C were almost the same as those of the composite fibers. The surface morphology of LaCrO₃ nanofibers became coarse with the increase of calcination temperatures. LaCrO₃ porous hollow nanofibers formed by nanoparticles were acquired at 600°C-900°C. SEM analysis indicated that the diameters of the synthesized LaCrO₃ nanofibers were in the range of 500-800nm, and their lengths were greater than 100μm. The diameters of LaCrO₃ nanofibers were smaller than those of the PVP/[La(NO₃)₃+Cr(NO₃)₃] composite fibers owing to the decomposition and evaporation of PVP and NO₃⁻.

3.3 FTIR spectra analysis

Pure PVP, PVP/[La(NO₃)₃+Cr(NO₃)₃] composite fibers and LaCrO₃ nanofibers(obtained by calcination of the PVP/[La(NO₃)₃+Cr(NO₃)₃] composite fibers at 900°C for 10h) were analyzed by FTIR, as shown in Figure 4. As seen from Figure 4, PVP(Figure 4a) and PVP/[La(NO₃)₃+Cr(NO₃)₃] composite fibers(Figure 4b) had the identical spectra, but absorption peaks intensity of spectrum for PVP/[La(NO₃)₃+Cr(NO₃)₃] composite fibers was lower than those of spectrum for pure PVP. This resulted from the lower content of PVP in the PVP/[La(NO₃)₃+Cr(NO₃)₃] composite fibers. All absorption peaks were attributed to PVP at 3438cm⁻¹, 2956cm⁻¹, 1662cm⁻¹, 1424cm⁻¹, and 1290cm⁻¹, corresponding to the stretching vibrations of hydroxyl group(ν_{O-H}), C-H bond(ν_{C-H}), carbonyl group($\nu_{C=O}$), C-H bond(ν_{C-H}), and C-N bond or C-O bond(ν_{C-N} or ν_{C-O}), respectively. It was seen from Figure 4c that all peaks of PVP disappeared, and at low wave number range, new absorption peaks at 598 and 415cm⁻¹ were appeared. The new absorption peaks were ascribed to the vibration of metal-oxygen bond, indicating that LaCrO₃ was formed. The results of FTIR analysis were in good agreement with XRD results.

3.4 Possible formation mechanism of LaCrO₃ porous hollow nanofibers

Possible formation mechanism of LaCrO₃ porous and hollow nanofibers was described as follows(as indicated in Figure 5). La(NO₃)₃·6H₂O, Cr(NO₃)₃·9H₂O and PVP were mixed with distilled water to form sol with certain viscosity. PVP acted as template during the formation processing of LaCrO₃ nanofibers. La³⁺, Cr³⁺ and NO₃⁻ were mixed with or absorbed onto PVP molecules to fabricate PVP/[La(NO₃)₃+Cr(NO₃)₃] composite fibers under electrospinning. During calcination treatment of the composite fibers, solvent water containing La³⁺, Cr³⁺, and NO₃⁻ ions in the composite fibers would remove to the surface of the PVP/[La(NO₃)₃+Cr(NO₃)₃] composite fibers and eventually evaporated from the composite fibers. Thus, La³⁺, Cr³⁺, and NO₃⁻ ions were also removed to the surface of the composite fibers brought by removed water. With the increasing in calcination temperature, PVP, and NO₃⁻ would oxidize and volatilize rapidly, La³⁺ and Cr³⁺ were oxidized into LaCrO₃ crystallites, and many crystallites were combined to form small LaCrO₃ nanoparticles, and these nanoparticles were mutually connected to generate hollow-centered and porous LaCrO₃ nanofibers. It was found from experiments that the average molecular weight of PVP and PVP content in the starting mixed sol had important impact on the formation of LaCrO₃ porous hollow

nanofibers. Further work is in progress.

4. Conclusions

4.1 PVP/[La(NO₃)₃+Cr(NO₃)₃] composite fibers were fabricated by electrospinning. Polycrystalline LaCrO₃ nanofibers were synthesized by calcining the relevant composite fibers at 600-900°C.

4.2 XRD analysis revealed that the composite fibers were amorphous in structure. The crystal structure of LaCrO₃ nanofibers was orthorhombic system with space group Pbnm.

4.3 SEM micrographs indicated that the surface of the prepared composite fibres was smooth, and the diameters of the composite fibres were in the range of 1-3µm. The diameters of LaCrO₃ nanofibers were smaller than those of the composite fibers. The surface of the LaCrO₃ nanofibers became coarse with the increase of calcination temperatures. LaCrO₃ porous and hollow nanofibers formed by nanoparticles were acquired when calcining temperature was 600-900°C. The diameters of LaCrO₃ nanofibers were in the range of 500-800nm, and their lengths were greater than 100µm.

References

- Dong, X. T., Guo, Y. Z., Yu, D. C., et al. (1994). Synthesis and electrical properties of LaCrO₃ nanometer powder. *Chin. J. Mater. Res.*, 8(3), 263-266.
- Duan, X. F., Huang, Y., Agarwal, R., Lieber, C. M. (2003). Single-nanowire electrically driven lasers. *Nature*, 421, 241-245.
- Hu, X. K., Qian, Y. T., Song, Z. T., et al. (2008). Comparative study on MoO₃ and H_xMoO₃ nanobelts: structure and electric transport. *J. Chem Mater*, 20(4), 1527-1533.
- Huynh, W. U., Dittmer, J. J., Alivisatos, A. P. (2002). Hybrid nanorod-polymer solar cells. *Science*, 295, 2425-2427.
- Iijima, S. (1991). Helical microtubules of graphitic carbon. *Nature*, 354, 56-58.
- Johnson C., Gemmen R., Orlovskaya N. (2004). Nano-structured self-assembled LaCrO₃ thin film deposited by RF-magnetron sputtering on a stainless steel interconnect material. *Composites Part B: Engineering*, 35(2), 167-172.
- Kar, S., Chaudhuri, S. (2006). Shape selective growth of CdS one-dimensional nano-structures by a thermal evaporation process. *J. Phys. Chem. B*, 110(10), 4542-4547.
- Li, D., Xia, Y. N. (2004). Direct fabrication of composite and ceramic hollow nanofibers by electrospinning. *Nano Lett.*, 4(5), 933-938.
- Li, D., Xia, Y. N. (2004). Electrospinning of Nanofibers: Reinventing the Wheel. *Adv. Mater.*, 16(14), 1151-1170.
- Mohapatra, S. K., Misra, M., Mahajan, V. K., et al. (2008). Synthesis of Y-branched TiO₂ nanotubes. *Materials Letters*, 62, 1772-1774.
- Morales, A. M., Lieber, C. M.(1998). A laser ablation method for the synthesis of crystalline semiconductor nanowires. *Science*, 279, 208-211.
- Pan, Z. W., Dai, Z. R., Wang, E.L. (2001). Nanobelts of semiconducting oxides. *Science*, 291, 1947-1949.
- Shao, C. L., Guan, H. Y., Liu, Y. C., et al. (2004). A novel method for making ZrO₂ nanofibres via an electrospinning technique. *J. Crystal Growth*, 267, 380-384.
- Shi, W. S., Zheng, Y. F., Wang, N., et al. (2001). A general synthetic route to III-V compound semiconductor nanowires. *Adv. Mater.*, 13, 591-594.
- Yang, Q. H., Fu, X. X. (2003). Analysis of photocatalytic oxidation activity of nano-LaMO₃(M=Cr, Mn, Fe, Co) compounds. *J. Chin. Ceram. Soc.*, 31(3), 254-256.
- Zhang B. Q., Li S. L., Sun LC. , et al. (2005). Preparation of doped lanthanum chromites nano-powders by aqueous organic-gel method. *J. Chin. Ceram. Soc.*, 33(4), 447-451.
- Zhang, S. H., Dong, X. T., Xu, S. Z., et al. (2007). Preparation and characterization of TiO₂@SiO₂ submicron-scaled

coaxial cables via a static electricity spinning technique. *Acta Chimica Sinica*, 65(23), 2675-2679.

Zhang, S. H., Dong, X. T., Xu, S. Z., et al. (2008). Preparation and characterization of $\text{TiO}_2/\text{SiO}_2$ composite hollow nanofibers via an electrospinning technique. *Acta Materiae Compositae Sinica*, 25(3), 138-143.

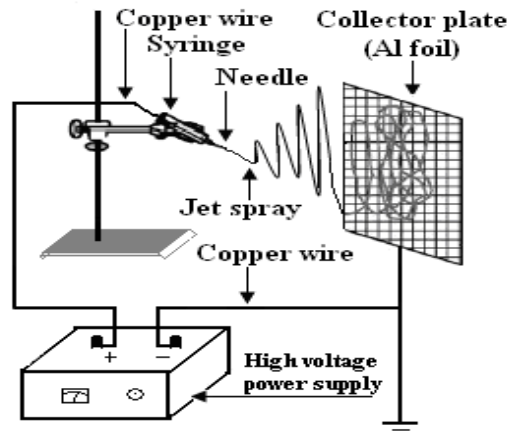


Figure 1. Schematic diagram of electrospinning setup

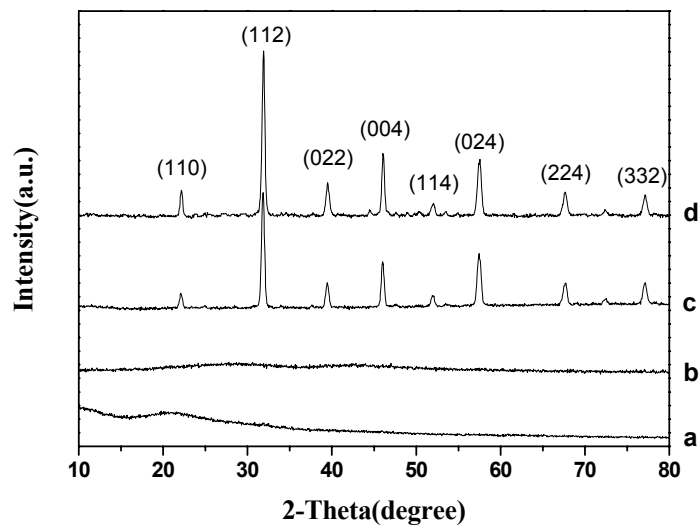


Figure 2. XRD patterns of samples

a. PVP/[$\text{La}(\text{NO}_3)_3 + \text{Cr}(\text{NO}_3)_3$] composite fibers b. 300°C c. 600°C d. 900°C

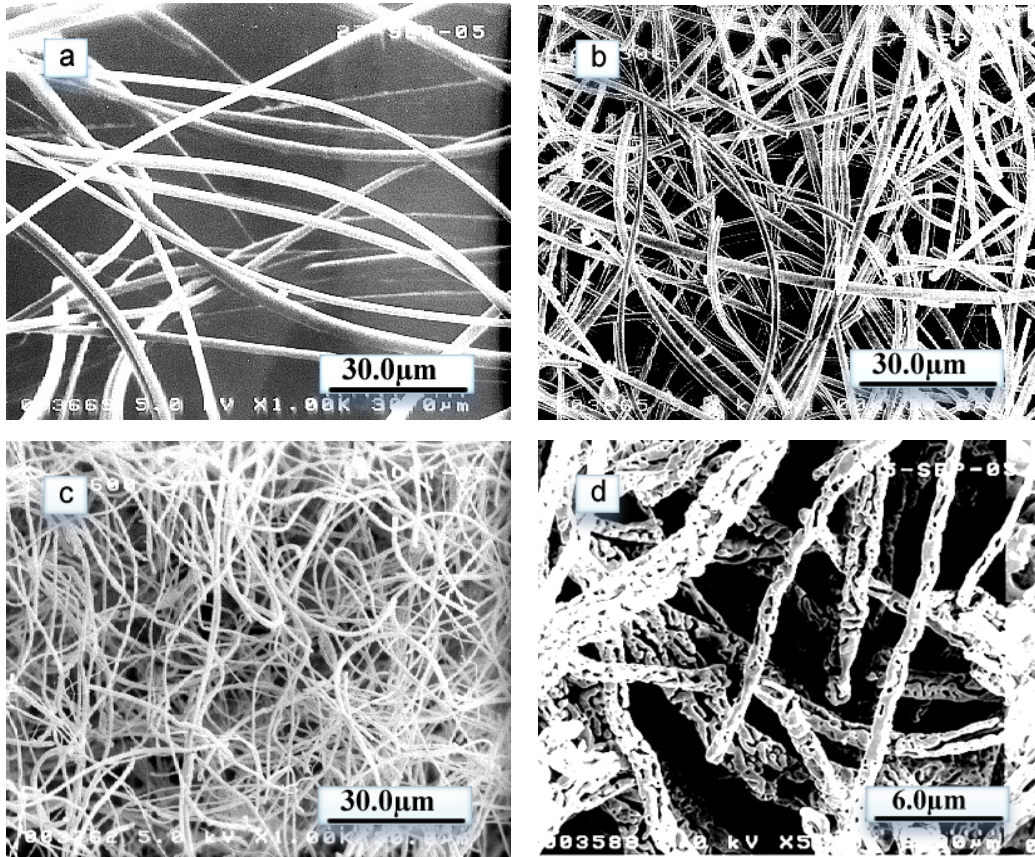


Figure 3. SEM micrographs of the fibers obtained at different temperatures
 a. PVP/[La(NO₃)₃+Cr(NO₃)₃] composite fibers b. 300°C c. 600°C d. 900°C

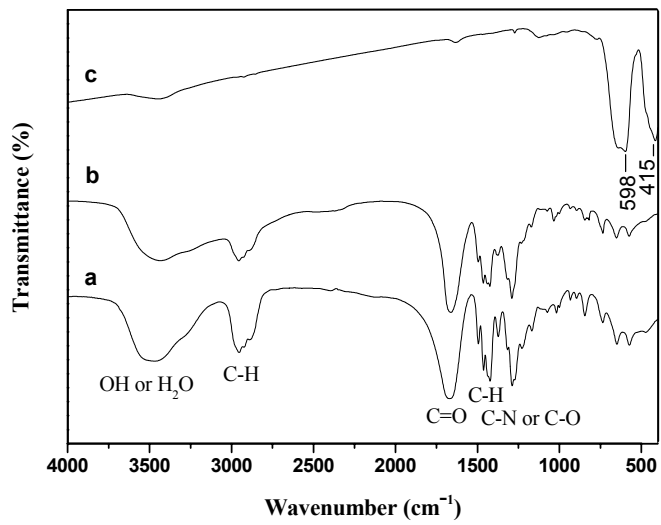


Figure 4. FTIR spectra of the samples
 a. PVP b. PVP/[La(NO₃)₃+Cr(NO₃)₃] composite fibers c. LaCrO₃ nanofibers

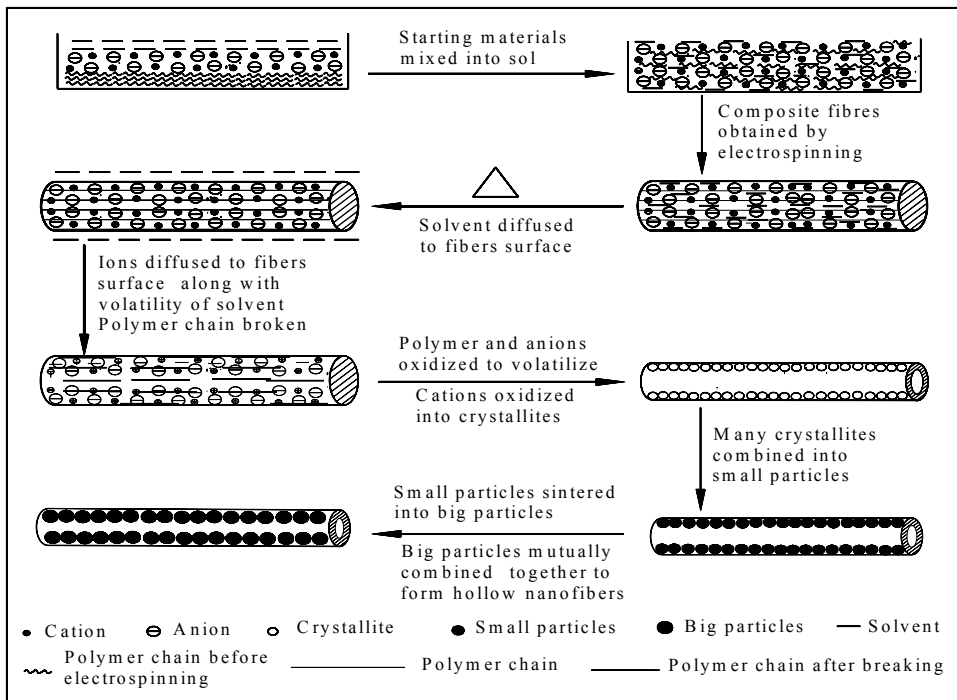


Figure 5. Illustrative diagram of possible formation mechanism of LaCrO_3 porous hollow nanofibers



Mapping of Individual Oil Palm Trees Using Airborne Hyperspectral Sensing: An Overview

Kamaruzaman Jusoff

Yale University, Yale's Centre for Earth Observation

Environmental Science Centre

21 Sachem St, New Haven, CT 06511, USA

Tel: 203-432-1384 E-mail: jusoff.kamaruzaman@yale.edu

Mubeena Pathan

Department of Forest Management, Faculty of Forestry, Universiti Putra Malaysia

UPM Serdang 43400, Selangor, Malaysia

Tel: 60-17-2645919 E-mail: pathanmubeena@yahoo.com

Abstract

This overview represents a preamble step for developing an approach for mapping individual oil palm trees from airborne hyperspectral imaging. The study generally describes airborne hyperspectral sensors in different fields particularly in agriculture by comparing and analyzing their uniqueness for different applications. The emphasis is on the image processing in identifying and mapping of the individual oil palm trees with the utilization of image histogram to examine the RGB bands. An algorithm is design to discover the involvement of different materials in a single mixed pixel and converting it into a pure pixel. The techniques employ in this connection are Linear Spectral Mixture Analysis (LSMA), Mix to Pure Converter (MPC) and Euclidean Norm.

Keywords: Hyperspectral, Airborne, Image processing, Linear spectral mixture analysis (LSMA), Mix to pure converter (MPC), Euclidean norm

1. Introduction

Trees contribute the major role in economic growth of any country therefore Palms are one of the most well-known and extensively cultivated plant family. They have had an important function in our daily life for example it is used in beverages, building material, chemical or industrial products, cosmetics, feeds, furniture, fuel etc. Many products are derived from palm like palm oil, it is the form of edible vegetable oil obtained from the fruit of the oil palm tree and the second most widely produced edible oil, after soybean oil. Demand for palm oil is raising and expected to climb further, particularly for the use of biodiesel; it is promoted as a form of renewable energy that greatly reduces next emission of carbon dioxide into atmosphere, and decrease the impact of green house effect. Keeping this importance in view, this study is aimed at investigating the technological impacts on oil palm plantation using different techniques for example hyperspectral airborne remote sensing.

This review presents general idea of hyperspectral remote sensing, mapping oil palm trees and other species and observes the technological development. Hyperspectral Remote sensing, a new technology, in combination with a land information system is believed to be a good technique to assist the agricultural land and managers in making fast decisions. It is quite supportive for the researchers and scientists to explore environment, atmosphere, minerals, plantations and vegetations etc. It is a direct geo-referencing system that provides the ability to directly relate the collected data to remote sensing system to the earth and accurately measure the position.

It is also recognized as image spectroscopy. Generally physicist and chemists use this expertise of image spectroscopy in the laboratory for the detection of matter and their composition for over 100 years. In mid 80' geologists used it for the mapping of mineral. Discovery of material is actually depending on spectral coverage, spectral resolution, and signal to noise of spectrometer. The new system that merges both imaging and spectroscopy is hyperspectral remote sensing .It can be classified in two categories like multipectral and hyperspectral.

Multispectral imagery is produced by sensors that measure reflected energy within several specific sections (also called bands) of the electromagnetic spectrum. Multispectral sensors usually have between 3 and 10 different band measurements in each pixel of the images they produce. Examples of bands in these sensors typically include visible green, visible red, near infrared, etc. Landsat, QuickBird, and SPOT satellites are well-known satellite sensors that use multispectral sensors.

Hyperspectral sensors measure energy in narrower and more numerous bands than multispectral sensors. Hyperspectral images can contain as many as 200 (or more) contiguous spectral bands. The numerous narrow bands of hyperspectral sensors provide a continuous spectral measurement across the entire electromagnetic spectrum and therefore are more sensitive to subtle variations in reflected energy. Images produced from hyperspectral sensors contain much more data than images from multispectral sensors and have a greater potential to detect differences among land and water features. For example, multispectral imagery can be used to map forested areas, while hyperspectral imagery can be used to map tree species within the forest.

2. Hyperspectral remote sensing

Jiang et al. (2004) described that hyperspectral technology imaging spectrometry technology, is one of the important leading research fields of remote sensing. Since the first imaging spectrometer was produced in 1983, in less than 20 years, hyperspectral remote sensing technology has been successfully applied in many fields, and shown great potential and bright prospects (Vane and Goetz, 1993). However, up to now the research on processing and applications of hyperspectral remote sensing data has fallen far behind the research on sensors. Research on processing, analysis and information extraction of hyperspectral data should be strengthened to determine more useful information, make full use of the advantage and potential of hyperspectral remote sensing technology and promote the development of new and important technology (Mazer et al., 1988).

Remote sensing presents an important tool for explore, monitoring and analyzing vegetation, water ,soil and wetland system etc and data acquire from the aircraft and satellite platforms have been widely used for mapping and modification for the same. The image data obtained from hyperspectral sensor is composed of many very narrow contiguous spectral bands ranging through the visible, near Infra Red (IR), mid-IR, and Thermal IR portion of the electromagnetic spectrum. It collects more than 200 bands of data, to explain an effective and constructive reflective spectral of every pixel and spectral signature. Later than atmospheric and topographic effects are applied, examine and compare the images with field and laboratory reflectance and distinguish, map and analyze minerals related with the deposit. The analysis of remotely sensed data is performed using a variety of image processing techniques, including: analog (visual) image processing, and digital image processing. Analog and digital analysis of remotely sensed data seeks to detect and identify important phenomena in the scene. Once identified, the phenomena are usually measured, and the information is used in solving problems. Optimum results are often achieved using a synergistic combination of both visual and digital image processing.

Digital image processing is used for many applications, including: weapon guidance systems (e.g., the cruise missile), medical image analysis (e.g., x-raying a broken arm), nondestructive evaluation of machinery and products (e.g., on an assembly line), and analysis of Earth resources. This class focuses on the art and science of applying remote

sensing digital image processing for the extraction of useful Earth resource information. Earth resource information is defined as any information concerning terrestrial vegetation, soils, minerals, rocks, water, certain atmospheric characteristics, and urban infrastructure.

2.1 Airborne hyperspectral imaging for different applications

The most appropriate extensively used technology for mapping rationale is Airborne and spaceborne imagery (Neto, 2001). The miscellaneous knowledge obtains from airborne and spaceborne sensors utilize to resolve lots of problems in comprehensive study of the earth. A survey of a few sensors and existing imagery considered by the author the most relevant is also presented. The two main platforms used at typical altitudes of 250km to 400km are the American Space Shuttle and, for now, the Russian MIR orbital station. Both the Space Shuttle and the MIR stations permit human interaction onboard allowing quick decisions and intervention on physical related problems. Also, by flying at lower altitudes, these sensors obtain better resolution information of the surface, not to mention the possibility of using non-electronic photographic cameras.

The experiment carried out on space shuttle suitable for mapping MOMS (Modular Optoelectronic Multipectral scanner) because the extra advantage that it can take the simultaneous views of earth surface, beside taking the stereo images with smaller time delay between them so it can avoid sun angle variation and different illuminations of scenes (Ebner et al., 1988; Neto, 1993; and Kramer, 1994). The characteristics of these sensors and the resulting imagery and resolution are also summarized. Its suitability for mapping at local, regional and global scales is examined. Opto-electronic sensor imagery is becoming suitable for map production at scales that were until recently only possible with aerial photography. The fact that these sensors are mounted on airborne and spaceborne platforms has the additional advantage of allowing studies and the production of maps of the Earth's surface also on a global scale. Also, this kind of imagery is more stable than if mounted on low altitude aircrafts, the orientation methods being high-accurate modeling algorithms. Digital format is an advantage for data storage and permits the automation of most of the procedures necessary to implement to a map production procedure. However, the procedures needed for the radar data preparation are still more complex than for data acquired by passive sensors. Although the data studied in this study are expensive, once the whole map production system is installed and prepared to manipulate, the costs can be competitive, as well as the information given by the increasing amount and diversity of data available, which approximate the recent market demands.

The airborne thermal infrared hyperspectral imaging system, Spatially Enhanced Broadband Array Spectrograph System (SEBASS), was flown over Mormon Mesa, NV, to provide the first test of such a system for geological mapping in May 1999. Several types of carbonate deposits were identified using the 11.25-mm band. However, massive calcrete outcrops exhibited weak spectral contrast, which was confirmed by field and laboratory measurements. Because the weathered calcrete surface appeared relatively smooth in hand specimen, this weak spectral contrast was unexpected. (Kirkland et al., 2002) monitor that microscopic roughness not readily apparent to the eye has introduced both a cavity effect and volume scattering to reduce a spectral contrast. The macro roughness of crevices and cobbles may also have significant cavity effect. The Mormon Mesa site studied is approximately 6 miles west of Mesquite, NV (latitude 36.45° , longitude 114.15°). The study focused on the adequate use of airborne hyperspectral to detect and characterise of unexpected effects that are not reproduced in standard laboratory measurements. The centre of the study is to minimize the instrumental supplies whenever possible. The effect of weather on the object that makes the field signature feeble at this time it is necessity when construe spectral data, consider the feeble signature introduce by the possible presence of lower spectral contrast material. In this research (Kirkland et al., 2002) differentiated between the three activities of remote sensing i.e. detection, discrimination and identification astonishingly. Detection involves a spectral signal that is consequential above the noise level, discrimination is spectral signal to detectable and difference from adjacent material and identification is both discrimination and a spectral band. For example, remotely sensed spectra may be converted to apparent emissivity and compared to laboratory spectra scaled in emissivity (Kahle and Alley, 1992). Emissivity is the measured radiance divided by the blackbody radiance at the target kinetic temperature. When the true target temperature is not known, it must be estimated, and apparent emissivity is the measured radiance divided by the blackbody radiance calculated at the estimated target temperature (Conel, 1969). The results demonstrate critical importance of exceeding the

minimum defined instrument requirements whenever possible. If the objectives include identification of materials that may be weathered and/or rough, then it should be remembered that the field signature of these materials is likely to be weak. This effect should be studied further using field and airborne hyperspectral instruments with sufficient sensitivity and spectral resolution to ensure detection and characterization of unexpected effects that are not reproduced in standard laboratory measurements. These steps are required to ensure instrumentation that will meet the SNR and spectral resolution necessary to detect and identify desired field materials. When interpreting spectral data, it is essential to consider the uncertainties introduced by the possible presence of lower spectral contrast materials, and the possibility that targeted materials may be missed entirely.

Hyperspectral remote sensing data with bandwidth of nanometer (nm) level have 10 or even several 100 of channels and contain abundant spectral information. Therefore, different channels have their own properties and show the spectral characteristics of various objects in the image. Rational feature selection from the varieties of channels is very important for effective analysis and information extraction of hyperspectral data. The site of the study was Shunyi region of Beijing, comprehensively analyzed the spectral characteristics of hyperspectral data. On the basis of analyzing the information quantity of bands, correlation between different bands, spectral absorption characteristics of objects and object separability in bands, a fundamental method of optimum band selection and feature extraction from hyperspectral remote sensing data was proposed. Feature selection is one of the most important steps in recognition and classification of remote sensing images. It is impossible to classify an image accurately and effectively without rational and efficient feature selection. This is especially important for hyperspectral remote sensing data (Mausel, 1990; Price, 1994; and Hsu and Tseng, 1999). Abundance in spectral information and power in distinguishing objects are the advantages of hyperspectral data. But, it does not mean that the more bands are used, the better because of the following points. There is evident correlation between bands, will destroy the normal distribution of spectra and influence the classification accuracy. If all the bands are used in classification without selection, the classification precision will decrease instead of increase. Second, the more bands are selected, the more training samples are needed to classify correctly. It is very difficult for hyperspectral data to find sufficient and correct training samples that can meet the demand of the classifier if too many bands are chosen in classification. Third, increase of band number in classification will inevitably result in the increase of processing time and cost that will reduce the processing speed and benefit. Since hyperspectral remote sensing data is rich in spectral information, thus evaluating and selecting optimal feature parameters for a concrete application goal is very important to make full use of such information in hyperspectral data and recognizing objects effectively and accurately.

The evaluation of new neural network classifier introduced by (Wang et al., 2007) by using spectrally sampled image data to map mixed halophytic vegetation in tidal environments. The work is based on the concept of vegetation communities, mixtures of several species, characteristic of salt marshes. The study site is the Venice lagoon, and the material available is a spectrally sampled Compact Airborne Spectral Imager (CASI) image, in conjunction with ground truth for precise characterization of vegetation communities. Detailed observations of vegetation species and of their fractional abundance were collected for 36 Regions of Interest (ROI): such field polygons are used for classification training and accuracy assessment. To select the most significant spectral channels, the Spectral Reconstruction method was applied to the image data: a set of 6 bands was selected as optimal for classification, out of the 15 available. The spatial heterogeneity of salt-marsh vegetation is significant and even at the spatial resolution of the airborne CASI image data, mixed pixels are observed. The Vegetation Community based Neural Network Classifier (VCNNC) is introduced to cope with a situation where no pure pixels exist, and was applied to the set of 6 selected bands. Both quantitative and qualitative comparisons of classification results of VCNNC with those of conventional Neural Network Classifier (NNC) trained and assessed on exactly the same data sets. Land cover mapping using spectral data relies on the relationship established between radiometric data (attributes) and independent observations of target (land cover) attributes and does not necessarily require the most radiometrically accurate at-surface data. There are for example indications that, in particular, atmospheric corrections on airborne-acquired image may not lead to higher classification accuracy (Hoffbeck and Landgrebe, 1994). The developed method then applied an approach for mapping highly mixed vegetation in salt marshes. The approach includes the use of methodologies to identify the spectral features containing the largest amount of information and the application of a Neural Network classifier to produce vegetation maps. The Spectral Reconstruction method,

based on the spectral information content, was chosen for optimal band selection. The application of this method to at-sensor CASI radiances extracted from training pixels showed that the information required for optimal vegetation mapping is contained in a subset of 6 spectral bands. These results are confirmed by experiments performed on the at-sensor radiance simulated from detailed high spectral resolution field measurements, which yielded a very similar set of selected bands. The coherence between results from airborne remotely-sensed and field observations indicates that little influence of atmospheric effects should be expected on the procedure of band selection.

Neural Network methods were preferred because they are capable of handling large amounts of data and do not require simplifying hypotheses on the statistical distribution of radiometric attributes. The Vegetation Community based Neural Network Classifier (VCNNC) was introduced. VCNNC training makes use of the detailed knowledge of intra-pixel fractional content of vegetation species (defining a particular vegetation community with a certain field polygon). Thus, VCNNC does not require “pure” training pixels, contrary to traditional classification methods, such as Maximum Likelihood and the usual Neural Network Classifiers (NNC). This circumstance is important in salt-marsh areas, where vegetation distribution can be heterogeneous at the pixel scale, thus leading to highly-mixed pixels.

The results in this case illustrate that the overall classification accuracy of VCNNC is 91.6% and only 84.17% for NNC. Furthermore, accuracy analysis applied to the two classification results shows a smaller classification error for VCNNC compared to NNC, and that the classification accuracy difference is related to the mixture degree: larger differences correspond to a higher mixing degree of the vegetation community. In other words, training dataset based on actual fractional abundance of species within a vegetation community used for neural network training leads to better classification results than those obtained using a training dataset which arbitrarily defines pure pixels on the basis of a majority rule. Moreover, the VCNNC provides sub-pixel fractional abundance of vegetation species, rather useful information for studies of salt-marsh ecology. However, since VCNNC is a supervised classification for working with areas of mixed vegetation, detailed and careful field-work is necessary for acquiring the accurate information of training samples in order to get reliable classification results.

2.2 Comparative analysis of airborne hyperspectral sensors

The Imaging Spectrometer Data Analysis System (ISDAS) developed by the Canada Centre for Remote Sensing and MacDonald Dettwiler and Associates on Sun Microsystems SPARC workstations using the Application Visualization System (AVS) software package to meet the requirements for efficient processing and analysis of hyperspectral data acquired with airborne as well as future spaceborne sensors. Various visualization tools have been developed for rapid exploratory analysis together with preprocessing and information extraction tools for numerical analysis. Linkages to a spectral database and a conventional image analysis system were established to support the analysis. (Staenz et al., 1997) express that, ISDAS is being used for multidisciplinary applications development in areas such as agriculture, environment, and exploration geology using physically based analysis approaches to retrieve information from hyperspectral data. This continuing effort, in collaboration with industry will lead to streamlined procedures that are important to take hyperspectral satellite remote sensing towards an operational mode.

An overview of this study is that the integrated system is designed to process airborne data, as well as data acquired by future spaceborne imaging spectrometers incorporating the simulation of future sensor data in the spectral domain from existing hyperspectral sensor data. With these objectives in mind, various visualization tools have been developed together with data input/output, preprocessing, and information extraction tools, and linkages to a spectral database and a conventional image analysis software package. These tools provide the functionalities to go from calibrated data to surface reflectance, to interactively view and analyze data, to extract qualitative and quantitative information, and to output results. They have been applied to CASI, FLI, SF%, and AVIRIS data in areas such as forestry, agriculture, and environmental monitoring and assessment. The tools are built into AVS, a commercial graphics software product running on Sun Microsystems SPARC workstations. This software environment is based on a modular design that guarantees the necessary flexibility for further modifications and additions with respect to future sensor data and related data processing technologies. Borner et al. (2001) emphasized that consistent end-to-end simulation of airborne and spaceborne earth remote sensing systems is an important task, and sometimes the only way for the adaptation and optimisation of a sensor and its observation conditions, the choice and test of

algorithms for data processing, error estimation and the evaluation of the capabilities of the whole sensor system. The presented software simulator SENSOR (Software Environment for the Simulation of Optical Remote sensing systems) includes a full model of the sensor hardware, the observed scene, and the atmosphere in between. The simulator consists of three parts. The first part describes the geometrical relations between scene, sun, and the remote sensing system using a ray-tracing algorithm. The second part of the simulation environment considers the radiometry. It calculates the at-sensor radiance using a pre-calculated multidimensional lookup-table taking the atmospheric influence on the radiation into account. The third part consists of an optical and an electronic sensor model for the generation of digital images. Using SENSOR for an optimization requires the additional application of task-specific data processing algorithms. The principle of the end-to-end-simulation approach is explained, all relevant concepts of SENSOR are discussed, and first examples of its use are given. The verification of SENSOR is demonstrated. This work is closely related to the Airborne PRISM Experiment APEX., an airborne imaging spectrometer funded by the European Space Agency.

This module describes the hardware of the remote sensing system considering the aspects of signal and system theory (Jahn and Reulke, 1995). It is divided in to an optical and an electronic part. The aim is the calculation of digital numbers from the at-sensor radiance given either by the radiative transfer module of SENSOR or by radiance values provided by other hyperspectral remote sensing systems. The complex end-to-end simulation tool SENSOR has been presented in this study. It allows modeling a large variety of optoelectronic remote sensing systems due to its modular and open structure. SENSOR includes models for the sensor hardware itself, the observed scene, and the atmosphere. Advanced features are implemented, e.g. ray tracing, fast and flexible access to atmospheric LUTs, sky view factor, point-spread function, and noise sources. With this tool, the interactions between parameters of the object–environment–sensor system, data processing, and output quantities, such as data accuracy and costs, can be evaluated.

Mustapha and Hutton (2001) in their study of position and orientation measurement systems used to directly georeference airborne imagery data, and present the accuracies that are attainable for the final mapping products. The Applanix Position and Orientation System for Airborne Vehicles (POS/AVTM) has been used successfully since 1994 to georeference airborne data collected from multispectral and hyperspectral scanners, LIDAR's, and film and digital cameras. The POS/AVTM uses integrated inertial/GPS technology to directly compute the position and orientation of the airborne sensor with respect to the local mapping frame. A description of the POS/AVTM system is given, along with an overview of the integrated inertial/GPS processing. An error analysis for the airborne direct geo-referencing technique is then presented. Firstly, theoretical analysis is used to determine the attainable positioning accuracy of ground objects using only camera position, attitude, and image data, without ground control. Besides theoretical error analysis, a practical error analysis was done to present actual results using only the POS data plus digital imagery without ground control except for QA/QC. The consequence of this investigate that the use of POS/AV enables a variety of mapping products to be generated from airborne navigation and imagery data without the use of ground control. The Applanix POS/AVTM direct geo-referencing system (Figure 1) is comprised of four main components: an IMU, a dual frequency low-noise GPS receiver, a computer system (PCS) and a post-processing software suite called POSpacTM. The heart of the system however is the Integrated Inertial Navigation software that is implemented both in real-time on the PCS and in post-mission using the POSpacTM software. In POSpacTM, the GPS measurements are used to aid the inertial navigation solution produced by integrating the IMU outputs to produce a blended position and orientation solution that retains the dynamic accuracy of the inertial navigation solution but has the absolute accuracy of the GPS.

<<Figure 1. Applanix POS/AVTM direct georeferencing system>>

A concise description of the concept of airborne remote sensing without ground control has been introduced through Applanix's POS systems. The basic concepts of inertial GPS integration have been described, along with the accuracy that can be achieved using such techniques. Then the ground accuracy using POS integrated with a digital frame camera was analyzed. The results show that direct geo-referencing can be used to obtain digital orthophotos to an accuracy that can meet many remote sensing requirements. Meanwhile, MultiSpec is a multispectral image data analysis software application designed by Biehl and Landgrebe (2002). It is intended to provide a fast, easy-to-use

means for analysis of multispectral image data, such as that from the Landsat, SPOT, MODIS or IKONOS series of Earth observational satellites, hyperspectral data such as that from the Airborne Visible–Infrared Imaging Spectrometer (AVIRIS) and EO-1 Hyperion satellite system or the data that will be produced by the next generation of Earth observational sensors. The primary purpose for the system was to make new, otherwise complex analysis tools available to the general Earth science community. It has also found use in displaying and analyzing many other types of non-space related digital imagery, such as medical image data and in K-12 and university level educational activities. MultiSpec has been implemented for both the Apple Macintoshes and Microsoft Windows operating systems (OS). The effort was first begun on the Macintosh OS in 1988. MultiSpec had its origin in the LARSYS multispectral image analysis system (Phillips, 1973), which was one of the first remote sensing multispectral data processing systems, originally created during the 1960s. (Larry,david 2002) express that multiSpec recognizes several header formats including ArcView, ENVI, ERDAS 7.3 and 7.4 *.lan and *.gis, ERDAS Imagine (4, 8 and 16-bit uncompressed), FastL7A, GAIA, GeoSPOT, GeoTIFF and TIFF uncompressed, HDF-Scientific Data Model (if all in one file), Land Analysis System (LAS), LARSYS Multispectral Image Storage Tape (MIST), LGSOWG, MacSADIE, MultiSpec ASCII classification, PDS, Sun “Screen Dump”, TARGA uncompressed and VICAR formats. MultiSpec also recognizes ArcView shape files. These capabilities of Multispec provide a state-of-the-art capability to analyze moderate and high-dimensional multispectral data sets of practical size.

The increasing number of sensor types for terrestrial remote sensing has necessitated supplementary efforts to evaluate and standardize data from the different available sensors. In this study (Soudani et al., 2006) access the potential use of IKONOS, ETM+, and SPOT HRVIR sensors for leaf area index (LAI) estimation in forest stands. In situ measurements of LAI in 28 coniferous and deciduous stands are compared to reflectance in the visible, near-infrared, and shortwave bands, and also to five spectral vegetation indices (SVIs): Normalised Difference Vegetation Index (NDVI), Simple Ratio (SR), Soil Adjusted Vegetation Index (SAVI), Enhanced Vegetation Index (EVI), and Atmospherically Resistant Vegetation Index (ARVI). The three sensor types show the same predictive ability for stand LAI, with an uncertainty of about 1.0m²/m² for LAI between 0.5 and 6.9m²/m². For each sensor type, the strength of the empirical relationship between LAI and NDVI remains the same, regardless of the image processing level considered [digital counts, radiances using calibration coefficients for each sensor, top of atmosphere (TOA), and top of canopy (TOC) reflectance]. On the other hand, NDVIs based on radiance, TOA reflectance, and TOC reflectance, determined from IKONOS radiometric data, are systematically lower than from SPOT and ETM+ data. The offset is approximately 0.11 NDVI units for radiance and TOA reflectance-based NDVI, and approximately 0.20 NDVI units after atmospheric corrections. The same conclusions were observed using the other indices. SVIs using IKONOS data are always lower than those computed using ETM+ and SPOT data. Factors that may explain this behavior were investigated. The key parameter ecosystem process is to provide attention to a large extent to LAI (Asner et al., 2003). Different ecophysiological development of a forest ecosystem are strongly controlled by LAI (Machado and Reich, 1999; Vargas et al., 2002) and interception of light (van Dijk and Bruijnzeel, 2001), gross productivity (Coyea and Margolis, 1994; Jarvis and Leverenz, 1983).

Based on simulations using the SAIL bidirectional canopy reflectance model coupled with the PROSPECT leaf optical properties model (i.e., PROSAIL), (Soudani et al 2006) demonstrated that the spectral response in radiance of IKONOS sensor in the red band is the main factor explaining the differences in SVIs between IKONOS and the other two sensors. IKONOS, ETM+, and SPOT HRVIR are among the most frequently used sensors for terrestrial applications. Given the subtle responses of canopies to environmental changes, and the small variations of canopy reflectance that are investigated, the intercomparison of these three sensors is an important task that may open new perspectives on spatial and temporal analyses of changes in forest canopies. Based on in situ measurements of LAI in 28 forest stands, the relationships established between LAI and SVI show that the three sensors have the same ability for LAI prediction. On average, the RMSE values from the different SVIs are very close ($\approx 1.0\text{m}^2/\text{m}^2$). On the other hand, SVIs determined using IKONOS radiometric data are systematically lower than those using SPOT and ETM+. The offset is about -0.11 for radiance and TOA reflectance-based NDVI, and about -0.21 after atmospheric corrections. Factors with the potential to explain these differences were evaluated based on simulations using the SAIL bidirectional canopy reflectance model coupled with the PROSPECT leaf optical properties model (i.e., PROSAIL). The analysis showed that: (a) Using radiance spectral responses from each of three sensors as inputs to

the PROSAIL model, IKONOS red reflectance is 53% higher than SPOT and ETM+. The IKONOS near-infrared band is 5% lower. The differences in the red band cause an average negative offset of IKONOS NDVI of about 0.08 for LAI ranging from 0.7 to 6.9m²/m². The spectral behavior of ETM+ and SPOT may be considered to be identical. (b) The gap between IKONOS and both SPOT and ETM+ for red reflectance and NDVI is LAI-dependent. It increases as LAI increases until the signal saturation threshold is reached (LAI≈4m²/m²).

Based on PROSAIL simulations, and by truncating the radiance spectral response of the IKONOS red band to match that of ETM+, the discrepancies between the two sensors in the red band and in the NDVI can be largely reduced and the output may be considered similar. It follows from these findings that the edge distortion in the red region of IKONOS spectral response in the red band is the main factor explaining the differences between this sensor and both SPOT and ETM+. Finally, (Soudani et al., 2006) concluded that for bare soils or surfaces covered by very sparse vegetation, radiometric data acquired by IKONOS, SPOT, and ETM+ are similar and may be used without any correction. For surfaces with dense vegetation, a negative offset of 10% of IKONOS NDVIs should be considered.

The part of a long-term effort to introduce precision viticulture in the region of Demarcated Region of Douro stated by (Morais et al., 2007) presents the architecture, hardware and software of a platform designed for that purpose, called MPWiNodeZ. A major feature of this platform is its power-management subsystem, able to recharge batteries with energy harvested from the surrounding environment from up to three sources. It allows the system to sustain operation as a general-purpose wireless acquisition device for remote sensing in large coverage areas, where the power to run the devices is always a concern. The MPWiNodeZ, as a ZigBee™ network element, provides a mesh-type array of acquisition devices ready for deployment in vineyards. In addition to describing the overall architecture, hardware and software of the monitoring system, the observation also reports on the performance of the module in the field, emphasizing the energy issues, crucial to obtain self-sustained operation. The testing was done in two stages: the first in the laboratory, to validate the power management and networking solutions under particularly severe conditions, the second stage in a vineyard. The measurements about the behavior of the system confirm that the hardware and software solutions proposed do indeed lead to good performance. The platform is currently being used as a simple and compact yet powerful building block for generic remote sensing applications, with characteristics that are well suited to precision viticulture in the DRD region. It is planned to be used as a network of wireless sensors on the canopy of vines, to assist in the development of grapevine powdery mildew prediction models. The feasibility of a ZigBee-based remote sensing network, intended for precision viticulture in the Demarcated Region of Douro. The network nodes are powered by batteries that are recharged with energy harvested from the environment. The power-management aspects have been found to be particularly critical, the main issues being the on-off cycles caused by partially charged batteries, and connectivity/network failures that lead to repeatedly unsuccessful connection attempts. Morais et al. (2007) designed the nodes to deal correctly with these issues, and tested the correctness of the solutions adopted by testing the nodes under particularly severe conditions. The testing and deployment of the devices was a two stage process. In the first stage, the devices were tested in the laboratory to validate the solutions that had been implemented, with particular emphasis on the power-management aspects.

The power consumption profiles measured during the tests validated the software-based solution, based on a finite state machine. The second and final stage was the deployment of a network of devices in the field a vineyard, with the cooperation of a winegrower. All results obtained so far confirm that the system works as envisaged, and operates reliably. Morais et al. (2007) concluded that the system nodes are able to sustain themselves based on solar energy alone; in other words, a ZigBee-based sensor network powered by batteries recharged by solar energy alone is feasible, if the networking and power-management issues are handled as proposed. No new hardware or software issues appeared when operating the system in the field. The system is in principle also able to harvest kinetic energy from wind and water in pipes. However, testing of these harvesting techniques has not been performed, for two reasons: first, these energy sources are more relevant to routers, which need a permanent energy supply, than to network nodes, which are less critical and can shut themselves off if necessary. Second, the performance of the nodes was main concern and the main purpose of our study. The system was endowed with the possibility of harvesting from both solar and kinetic energy sources in anticipation of future applications, including for example applications in

greenhouses. A router placed inside a greenhouse would clearly benefit from harvesting kinetic energy from water in pipes.

3. Computerization in image processing and quantifying of individual oil palm trees

Computer science is a vibrant and constantly evolving discipline, concerned with uncovering the laws of universe; obvious examples are physics, chemistry, mathematics, agriculture and environment. Research in this perspective spans a very wide spectrum of activities from information retrieval to animation and image processing. Computer vision is the construction of explicit, meaningful description of any physical object for example soil, wetland, tree etc from images. It is the enterprise of automating and integrating a wide range of processes and representation used for vision perception, including image processing and statistical pattern classification. Image analysis and computer vision constitute a broad and rapidly evolving field. The manipulation encompasses several types of processing techniques, collectively known as digital image or computer graphic; usually stand for a 2-D intensity function. It is represented by a matrix whose rows and columns identify a point in an image and matrix element value identify as a pixel. The consequence of image analysis is exceptionally valuable in the field of environment particularly for the counting of oil palm trees. Quantifying oil palm trees manually, is very time consuming and complex task, because many factors involve at this point for example physical and environmental conditions. Thus oil palm is a significant crop so this gigantic issue is necessary to resolve. So many researchers effort to work out this dilemma, recently high resolution IKONOS images have expanded which can have the accuracy to view the plantation from many angles. Dr Liew Soo Chin at the Centre for Remote Imaging, Sensing and Processing (CRISP) developed software which is supportive and optimal procedure for the monitoring and quantifying and modeling trees as shown in Figures 2 and 3.

Image processing and analysis procedure acquire a pace to achieve an objective. These including the raw data express accurate geographic location and geometric correction. Then image histogram is use to examine the three bands near infrared band displayed in red, red band displayed in green and green band displayed in blue .Subsequently image enhancement is used for visual interpretation. Afterward image classification is occurring according to brightness and color information of each pixel. These comprise of objects within the image likewise water, forest, shrubs etc. In high spatial resolution imagery, details such as buildings and roads can be seen. The amount of details depends on the image resolution. In very high resolution imagery, even road markings, vehicles, individual tree crowns, and aggregates of people can be seen clearly. Pixel-based methods of image analysis will not work successfully in such imagery. In order to fully exploit the spatial information contained in the imagery, image processing and analysis algorithms utilizing the textural, contextual and geometrical properties are required. Such algorithms make use of the relationship between neighboring pixels for information extraction. Incorporation of a-priori information is sometimes required. A multi-resolution approach (i.e. analysis at different spatial scales and combining the resolute) is also a useful strategy when dealing with very high resolution imagery. In this case, pixel-based method can be used in the lower resolution mode and merged with the contextual and textural method at higher resolutions. Individual trees in very high resolution imagery can be detected based on the tree crown's intensity profile. An automated technique for detecting and counting oil palm trees in IKONOS images based on differential geometry concepts of edge and curvature has been developed at CRISP, National University of Singapore.

<<Figure 2. Oil palm trees in an IKONOS image >>

<<Figure 3. Detected trees (white dots) superimposed on the image>>

3.1 Hyperspectral pixel detection

The hyperspectral image with spatial resolution is consisting of more than one material especially in the field of agricultural mapping. The plant image is generally composed of leaves, flower, fruit, stem, and ground and all these things reproduce reflection differently. Now for the quantification, at the initial stage it is necessity to design an algorithm to discover these materials and its involvement in each pixel and subpixel to detect the target. Priori model leads to posteriori approach is apply here, the main difference between these two approaches are that the abundance fractions generated by the priori model do not reflect true amounts of fractional images of the image pixel. In contrast of this posteriori model can estimate true amount of abundance fractions can used for target classification and material quantification (Chang, 2003) Linear Spectral Mixture Analysis(LSMA) is consider for detection of target

and evaluate with Nonnegative Constrained Matrix Factorization (NCMF).The NCMF is helpful to produce data in positive identification. Then evaluate PPC (Pure Pixel Converter) and MPCV (Mixed to Pure Converter) and finally use minimum distance based formula, the most favorable norm is Euclidean norm.

3.2 Linear spectral mixture analysis (LSMA)

LSMA is frequently used to emerge in Mixed Pixel Classification(MPC),in Linear mixing model, L is the spectral band and t_1, t_2, \dots, t_p , are targets. Where m_1, m_2, \dots, m_p , are target signature (endmember) also denoted by digital number, r is the hyperspectral pixel vector .linear combination of target m_1, m_2, \dots, m_p , and abundant fractions are $\alpha_1, \alpha_2, \dots, \alpha_p$. Suppose that r and M is $L \times 1$ column pixel vector and $L \times p$ target spectral matrix.

The model for spectral signature can be as follows:

$$r = M\alpha + n \tag{1}$$

Where n is the noise or can be construing as a measurement error, r is to indicate spectral signature.This is also known as Bayes or priori model.

In equation 1, α must be positive and added equal to 1:

$$\alpha_i \geq 0, \quad i=1, \dots, m. \tag{2}$$

$$\sum_{i=1}^m \alpha_i = 1 \tag{3}$$

When the material in a pixel are arranged just about each other like mixture of diverse natural resources(stone, granite, rocks),here the interaction of light is more than one material therefore the reflected value is closer to non linear combination of the reflection. The reflection of each material is different so linear mixing model does not work correctly. There are several techniques are formed for the estimation of $\alpha = (\alpha_1, \alpha_2, \dots, \alpha_p)^T$ directly from image (Settle, 1996; Tu et al., 1997; Chang et al. 1998) based on posteriori information given by:

$$\begin{aligned} r &= M \hat{\alpha} + \hat{n} \\ r &= d \hat{\alpha}_p + U \hat{\gamma} + \hat{n} \end{aligned} \tag{4}$$

$\hat{\alpha}, \hat{\alpha}_p, \hat{\gamma}$ are estimation of α, α_p , and γ , this is the posteriori abundance estimation model

3.3 Mix to pure converter (MPCV)

By comparing pure pixel converter (PPC) to Mix pixel converter (MPC), the estimated abundance vector $\hat{\alpha}$ must be pure abundance vector and there are only p choices for α .

Therefore it is assigned to solve the (MPC) problem only p class classification.

$$\chi_{MPCV}(r) = Mu_j = m_j \tag{5}$$

$$1 \leq j \leq p$$

$\chi_{MPCV}(r)$ is called mixed to pure pixel converter (MPCV),operating on a pixel vector r that assigns r to signature m_j for some j. The estimated noise \hat{n} is absorbed into u_j to account for misclassification error. Interpreting eq: 1 and eq: 5, each target signature vector in M represents a distinct class image pixel vector r will be assign to one signature of

M through MPCV. Now the binary image is formed and displays target pixels only. (Ren, 2000) suggested a method based on winner-take-all (WTA) thresholding criterion. Suppose there are p target signatures $\{m_j\}_{j=1}^p$

Where m_j is the jth signature and r be the mixed pixel vector to be classified and $\alpha(r) = (\alpha_1(r), \alpha_2(r), \dots, \alpha_p(r))$ estimated p-dimensional abundance vector. Estimated abundance fraction

$$\{\hat{\alpha}_1(r), \hat{\alpha}_2(r), \dots, \hat{\alpha}_p(r)\}$$

$$\chi_{WTAMPCV}(r) = \text{Mu}_{j^*} = m_{j^*} \tag{6}$$

$$j^* = \arg \left\{ \max_{1 \leq j \leq p} \left\{ \hat{\alpha}_j(r) \right\} \right\}$$

where $\hat{\alpha}_{j^*}(r) = 1$ and $\hat{\alpha}_j(r) = 0$ for $j \neq j^*$

The j^* -th p dimensional unit vector $u_{j^*} = (0, \dots, 0, 1, 0, \dots, 0)^T$

Where 1 indicate the value of j^*

With $j^* = \arg \left\{ \max_{1 \leq j \leq p} \left\{ \hat{\alpha}_j(r) \right\} \right\}$

3.4 Minimum distance classification

Due to the fact that noise is included as part of misclassification error, noise term is therefore excluded. The white Gaussian, the mixed pixel classifiers, OSP become unconstrained Gaussian maximum likelihood (GML) classifier,

$$\hat{\alpha}_{gml} = \arg \left\{ \max_{\alpha \in \Delta} p(r) \right\} \tag{7}$$

Where Δ is limited to the set $\Delta = \{u_j\}_{j=1}^p = \{(1, 0, \dots, 0)^T, (0, 1, \dots, 0)^T, \dots, (0, 0, \dots, 1)^T\}$

It contains only p unit vectors $\Delta = \{\hat{\alpha} = (\hat{\alpha}_1, \dots, \hat{\alpha}_p)^T\}$

$\hat{\alpha}_j = 1$ for some j, $\hat{\alpha}_i = 0$ for $i \neq j$

an image pixel vector r is assigned to m_{j^*}

$$\chi_{GML}(r) = \text{Mu}_{j^*} = m_{j^*} \tag{8}$$

Where $j^* = \arg \left\{ \min_{1 \leq j \leq p} \|r - m_j\| \right\}$

The most common type of distance based method used in sample statistics is Euclidean distance norm:

$$ED(x, m_j) = \sqrt{(x - m_j)^T (x - m_j)} = \sqrt{\sum_{i=1}^L (x_j - m_{ji})^2} \tag{9}$$

Figures 4 and 5 below illustrated the algorithm details and the framework involve in the advance processing of hyperspectral data.

<<Figure 4. Mix to Pure conversion algorithm>>

<<Figure 5. Framework of the assigned algorithm>>

The development of an algorithm is to make comparative analysis of the image .This algorithm is then implement in high level language and produce source code. This source code runs on the Intel Core 2 Duo system, it has 2.00GHz (4CPU), 1GB RAM.

4. Conclusion

Several hyperspectral and image analysis algorithms are developed for target detection in different field. It is very difficult to compare with each other because lack of standardized data. The main problem that there is no any particular rule and process strictly followed to provide information or evidence to prove the algorithm. The designed algorithm comprehend mixed pixel to pure pixel conversion by inflicting on target signature abundance fractions. In result the algorithm reduce to three classes, LSMA, MPC and distance based pure pixel. The WTA based converter use for tot up target pixel thresholding technique.

References

- Asner, G.P. Scurlock, G.M. and Hicke, J.A. (2003). Global synthesis of leaf area index observations: Implications for ecological and remote sensing studies. *Global Ecology and Biogeography*, 12, 91–205.
- Bheil, L. and Landgrebe, D. (2000). Multispec- a tool for multispectral -- hyperspectral image analysis. *Computer and Geosciences*, 28, 1153-1159.
- Börner, A. Wiest, L. Keller, P. Rulke, R. Ritcher, R. Schapman, M. and Schalpfer, D. (2001). SENSOR: a tool for the simulation of hyperspectral remote sensing. *ISPRS Journal of Photogrammetry & Remote Sensing*, 55, 299–312.
- Chang, C.I. (1998). A study on spectral characteristics for HYDICE data by spectral similarity and dissimilarity on a single pixel basis: *final report*. Desert Research Institute.
- Chang, C.I. (2003). *Hyperspectral Imaging: Techniques for Spectral Detection and Classification*. Kluwer Academic.
- Conel, J.E (1969). Infrared emissivities of silicates: Experimental Results and a Cloudy Atmosphere Model of Spectral Emission from Condensed Particulate Mediums. *Journal of Geophysical Research*, 74, 1614– 1634.
- Coyea, M.R. and Margolis, H.A. (1994). The historical reconstruction of growth efficiency and its relationship to tree mortality in balsam fir ecosystems affected by spruce budworm. *Canadian Journal of Forest Research*, 24, 2208–2221.
- Dijk, A.I.J.M. and Bruijnzeel, L.A. (2001). Modelling rainfall interception by vegetation of variable density using an adapted analytical model: Part 1. Model description. *Journal of Hydrology*, 247, 230–238.
- Ebner, H. Müller, F. and Zhang, S. (1988). Studies on Object Reconstruction from Space Using Three Line Scanner Imagery. *International Archives of Photogrammetry and Remote Sensing*, 27, 242-249.
- Hoffbeck, J.P. and Landgrebe, D.A. (1994). Effect of radiance-to-reflectance transformation and atmosphere removal on maximum likelihood classification accuracy of high-dimensional remote sensing data. *Proceedings of the International Geoscience and Remote Sensing Symposium*, 2538–2540.
- Hsu, P.H. and Tseng, Y.H (1999). *Feature extraction for hyperspectral image*. Proceedings of the 20th Asian Conference on Remote Sensing. Joint Laboratory for Geo Information Science of the Chinese Academy of Sciences and the Chinese University of Hong Kong, 405–410.
- Jiang, X. Tang, L. Wang, C.Y. and Wang, C. (2004). Spectral characteristics and feature selection of hyperspectral remote sensing data. *International Journal of Remote Sensing*, 25, 51–59.
- Jarvis, P.G. and Leverenz, J.W. (1983). Productivity of temperate deciduous and evergreen forest. Ecosystem processes: *Mineral cycling, productivity and man's influence*, 233–280.
- Kahle, A. and Alley, R. (1992). Separation of temperature and emittance in remotely sensed radiance measurements. *Remote Sensing of Environment*, 42, 107– 111.
- Kirkland, L. Hera, K. Kerin, E. Adams, P. Hackwell, J. and Teriman, A. (2002). First use of an airborne thermal infrared hyperspectral scanner for compositional mapping. *Remote Sensing of Environment*, 80, 447–459.
- Kramer, H.J. (1994). *Observation of the Earth and its environment: survey of missions and sensors*. 2nd editon. Springer-Verlag, Berlin

- Machado, J.L. and Reich, P.B. (1999). Evaluation of several measures of canopy openness as predictors of photosynthetic photon flux density in deeply shaded conifer-dominated forest understory. *Canadian Journal of Forest Research*, 29, 1438–1444.
- Mausel, P.W. Kamber, W.J. and Lee, J.K. (1990). Optimum band selection for supervised classification of multispectral data. *Photogrammetric Engineering and Remote Sensing*, 56, 55–60.
- Morais, R.F, M.A. Matos, S.G. Seradio, C. Ferreria, P.J.S.G. and Ries, M.J.C.S. (2007) A ZigBee multi-powered wireless acquisition device for remote sensing applications in precision viticulture. *Computers and Electronics in Agriculture*, 62, 94–106.
- Mustapha, M. and Hutton, J. (2001). Airborne Remote Sensing Without Ground Control. *IEEE Transaction on Geoscience and Remote Sensing Symposium*, 7, 2961-2963.
- Mazer, S.A. Martin, M. Lee, M. and Solomon, J.E. (1988). Image processing software for imaging spectrometry data analysis. *Remote Sensing of Environment*, 24, 201–211.
- Neto, F.A. (2001). *Airborne and Spaceborne Imagery for Mapping*. Ph.D Thesis, 119-126.
- Neto, F.A. (1993). *Analysis of the characteristics and orientation of linear array stereo imagery from satellite sensors*. Ph.D thesis. University of London.
- Phillips, T.L. (1973). *LARSYS User's Manual: Laboratory for Applications of Remote Sensing*. Purdue University. West Lafayette, Indiana. 118.
- Price, J.C. (1994). Band selection procedure for multispectral scanners. *Applied Optics*, 33, 3281–3288.
- Settle, J.J (1996). On the relationship between spectral unmixing and subspace projection. *IEEE Transaction on Geoscience and Remote Sensing*, 34, 1045-1046.
- Soudani, K. Francois, C. Maire, G. and Dantec, V. (2006). Comparative analysis of IKONOS SPOT, and ETM+ data for leaf area index estimation in temperate coniferous and deciduous forest stands. *Remote Sensing of Environment*, 102, 161–175.
- Staenz, K. Schwarz, J. and Cheriyian, J. (1997). *Processing Analysis/ Capabilities for Data Acquired With Hyperspectral Spaceborne Sensor*. Elsevier Science Ltd., 39, 923-931.
- Tu, T.M. Chen, C.H. and Chang, C.I. (1997). A posteriori least squares orthogonal subspace projection approach to weak signature extraction and detection. *IEEE Transaction on Geoscience and Remote Sensing*. 35, 127-139.
- Vane, G. and Goetz, A.F.H. (1993). Terrestrial imaging spectrometry: current status, future trends. *Remote Sensing of Environment*,. 44, 117–126.
- Vargas, L.A. Andersen, M.N. Jensen, C.R. and Jorgensen, U. (2002). Estimation of leaf area index, light interception and biomass accumulation of *Miscanthus sinensis* ‘Goliath’ from radiation measurements. *Biomass and Bioenergy*, 22, 1–14.
- Wang, C. Menenti, M. Stoll, M. Belluco, E. and Marani, M. (2007). Mapping mixed vegetation communities in salt marshes using airborne spectral data. *Remote Sensing of Environment*, 107, 559–570.

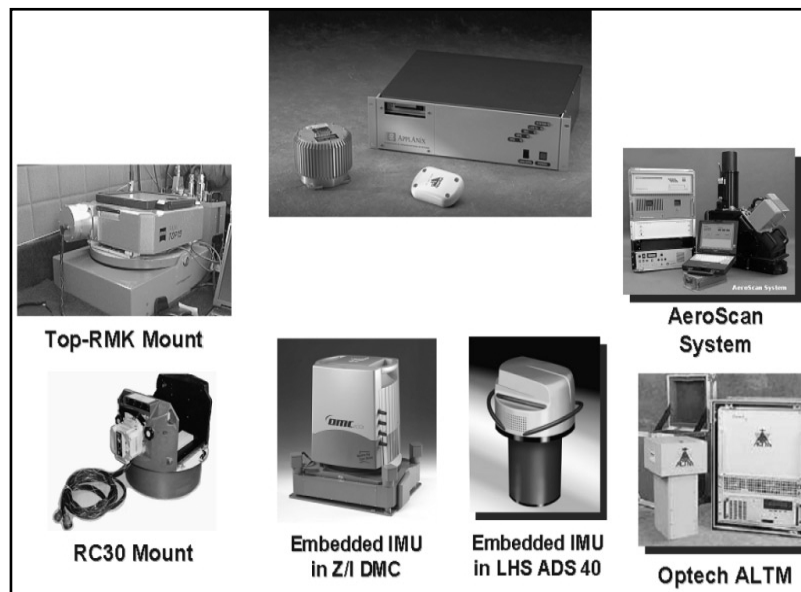


Figure 1. Applanix POS/AVTM direct georeferencing system

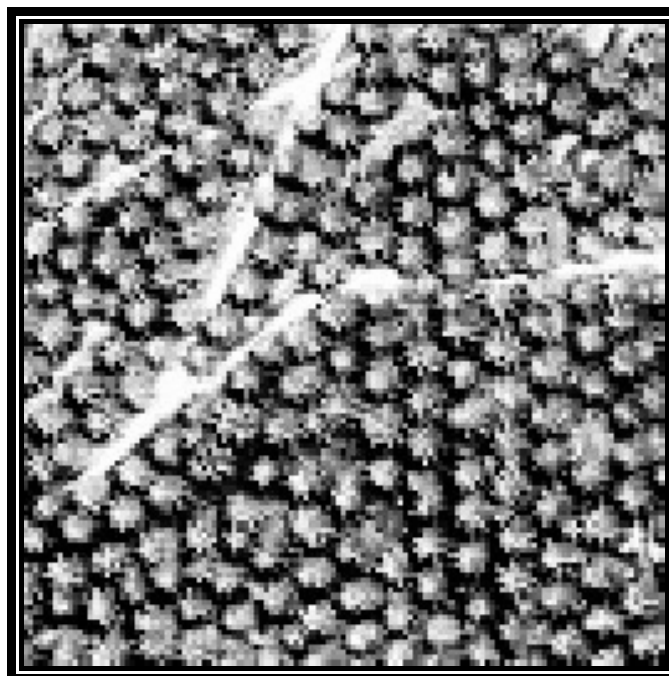


Figure 2. Oil palm trees in an IKONOS image

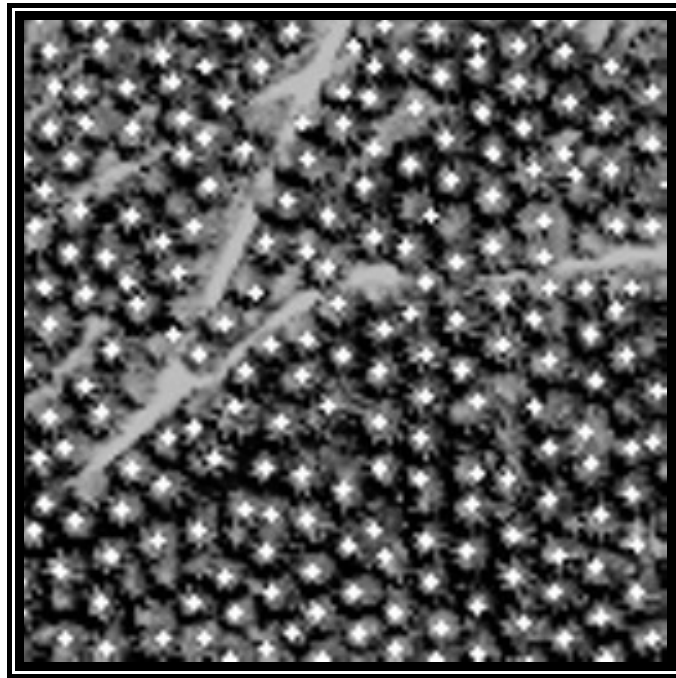


Figure 3. Detected trees (white dots) superimposed on the image

Algorithm:

1. Initialize positive value for hyperspectral pixel vector
2. Processing
3. Mix to Pure Pixel conversion
4. If pure pixel obtained
5. Start counting
6. Repeat

Figure 4. Mix to pure conversion algorithm

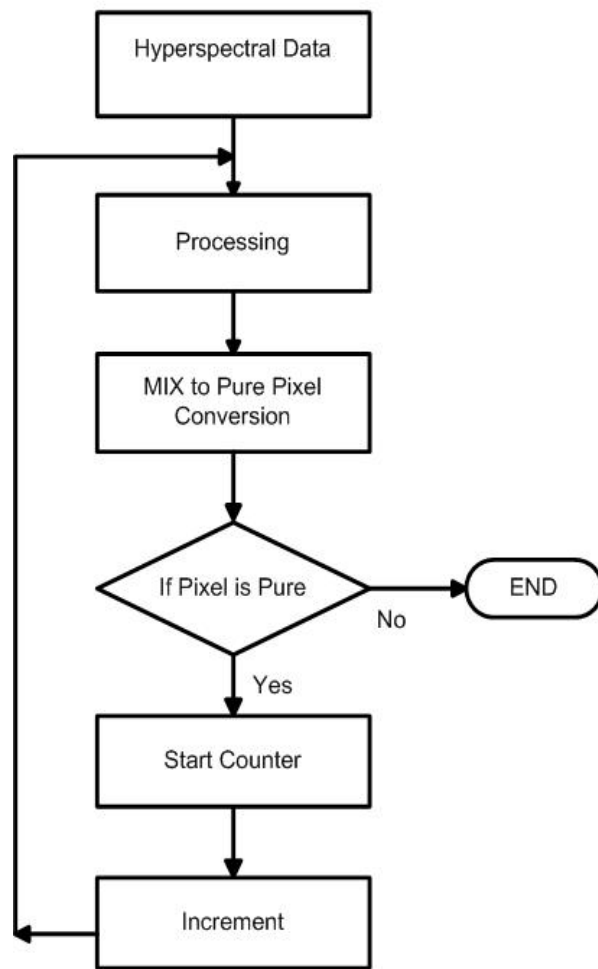


Figure 5. Framework of the assigned algorithm



Study on the Optimization Method of Transducer Linear Transmission Function Based on Structural Parameter Adjustment

Guangxu Lin

Chengdu University, Chengdu 610106, China

E-mail: 670149343@qq.com

Abstract

The basic task of the transducer is to convert non-electric physical quantity into electric physical quantity, and implement effective linearization processing to the acquired physical quantity and offer ideal data chain for later measurement circuit. The single variable transmission character of transducer is the quality attributes function about above tasks, which reflects the corresponding relation between input and output, i.e. the linearization degree between both physical quantities. Taking a sort of capacitance transducer as the sample, in this article, we put forward a sort of exact transmission character optimization method of single variable linear correlation analysis with strong operation feature based on the base of statistics. According to this method, for each sort of transducer, the correlation coefficient between output and input can be conveniently computed, and the linearization quality of transducer can be evaluated according to the correlation coefficients, and finally the transducer can achieve ideal linearization level through the adjustment of structure parameter, which can offer sufficient optimization space for the quantity transmission character and manufacturing techniques.

Keywords: Quantity transmission character, Optimization method, Linear correlation analysis, Correlation coefficient

1. Introduction

In the domain of autoimmunization detection technology, the transmission function between output and input of transducer is decided by not only the basic work principle of physics, but the concrete structure of transducer in the technical design, and the quality of the acquired transmission function is related with the correlation between output and input. For changes in the world, the change of one phenomenon always depends on the change of other phenomena, which is the correlation character among things. In theory, for any one transducer, its transmission function of physical quantity will always present obvious linear correlation character in certain value region, and it can be reflected by diagram or mathematical relation, and if the value region range contained by the linear correlation of this physical quantity is just consistent with the objective value region of the transducer, so it is the ideal situation. But in fact, both parties always are not completely consistent, or they are just partly consistent, i.e. in the value region what we needs, the transmission function is just linear in part of region, and in other parts of region, the correlation among physical quantities always presents complex nonlinear relationship, which will certainly brings difficulties for the later processing works after data acquisition, and if we can exactly grasp the quantity transmission character of the transducer in the phase of structure design, and make correlation evaluation ever and again, we can adjust the quantity transmission character in certain range through the structure adjustment, and implement effective prophase optimization for the latter application.

2. Quantity transmission character and representation form of transducer

In the physical world, the mutual relationships among natural phenomena are very complex, and they are restricted and influenced each other by different orientations, values and degrees. Concretely speaking, the attribute tokens of natural phenomena are mixed physical quantities, and in the development work of transducer, we should evaluate the correlation relationship between input and output, and primarily confirm whether there are obvious correlation relationships between them, and if rough linear correlation exists between them, we can find out the structure parameters which obviously influence the transmission function, and implement corresponding quantitative analysis. According to each data inputting into the function, we should make corresponding correlation diagram and correlation table, then we can directly judge the form of the transmission function and compute the correlation coefficient to implement quantitative analysis, which can exactly reflect their correlation relationships, and these correlation relationships are the quantity transmission character what we said. Generally speaking, the quantity transmission character of the transducer can be represented as two forms, i.e. the scatter diagram method and the correlation coefficient method.

2.1 Scatter diagram method

According to the acquired transducer input and output data table, take the measured physical quantity as the transverse axis and the output quantity as the longitudinal axis, label the data group one by one on the diagram, and the corresponding scatter diagram can be obtained. The scatter diagram method can clearly denote the correlation character between input and output of transducer (seen in Figure 1), but its precision is not high, and especially for the transducer which requires high linearization, this method can not be used to establish exact quantitative analysis platform.

In fact, many transducers based on same quantity transmission principle will always induce that scatter diagrams of their quantity transmission functions present different diagrams because of the tiny difference of geometric structure. For example, for two physical quantities x and y based on same quantity transmission principle, we can respectively plot their scatter diagrams on the $O-xy$ plane through data acquisition, and from the scatter diagram, we can see that because of the different structures of transducers, high linear correlation relationship, or low linear correlation relationship may present between them, and even nothing correlation are presented (seen in (a), (b), (c) of Figure 1).

2.2 Correlation coefficient method

The correlation coefficient method is a sort of exact quantitative analysis method in the research of transducer quantity transmission character, and its concrete analysis approaches include taking the acquired transducer input and output data table as the start, taking the measured physical quantity as the independent variable x , taking the output as the function y , then filling them into the standard deviation list one by one, and finally acquiring the linearization correlation coefficient r corresponding with the transducer by the product moment method in the statistics, and r will directly reflect the linearization degree of the transducer, and the change of structure parameter of every transducer will be denoted by r . The meaning of this method is that we can make certain adjustment to the structure parameter of the transducer according to the relative quantitative analysis between input and output, and convert the transmission function to the linear direction, and offer convenience for the linearization of signal processing of the measurement circuit. After the structure of the transducer is confirmed, the correlation coefficients are also confirmed. When the structure of the transducer is changed, the correlation coefficients are also changed. So we can optimize the correlation coefficients through adjusting the structure parameters of the transducer, and accordingly enhance the linearization degree of the transducer transmission character.

3. Acquisition of transducer correlation coefficients

According to the quantity transmission data table of transducer, we can utilize the product moment method or the EXCEL method in statistics to compute the correlation coefficient r . Taking the initial parallel flat structure (seen in Figure 3, and the corresponding quantity transmission data table is seen in Figure 1) of the capacitance solid particulate matter moisture transducer as the example, we introduce above two sorts of computation methods of correlation coefficient.

For the product moment method, first define x as the moisture content H (%) of the measured matter, and define y as the output capacitance Cx (pF) of the capacitance transducer, take the quartz sands with different moisture contents as the measured matters, acquire a series of original data and respectively them into the column x and the column y of the transducer standard deviation table, and then respectively compute corresponding $x - \bar{x}$, $y - \bar{y}$, $x - \bar{x}$, $y - \bar{y}$, $(x - \bar{x})^2$, $(y - \bar{y})^2$ and $(x - \bar{x})(y - \bar{y})$, and fill them in the table one by one (seen in Table 1).

Then, compute corresponding correlation coefficient by the following product moment method formula.

$$r = \frac{\sigma_{xy}^2}{\sigma_x \sigma_y} \quad (1)$$

Where,

$$\sigma_{xy}^2 = \frac{\sum (x - \bar{x})(y - \bar{y})}{n} \quad (2)$$

is called as the covariance of independent variable sequence and the attributive variable sequence.

$$\sigma_x = \sqrt{\frac{\sum (x - \bar{x})^2}{n}} \quad (3)$$

is called as the standard deviation of the independent variable sequence.

$$\sigma_y = \sqrt{\frac{\sum (y - \bar{y})^2}{n}} \quad (4)$$

is called as the standard deviation of the attributive variable sequence. So the correlation coefficient formula can be also denoted as

$$r_1 = \frac{\sum (x - \bar{x})(y - \bar{y})}{\sqrt{\sum (x - \bar{x})^2} \sqrt{\sum (y - \bar{y})^2}} = \frac{59.5264}{\sqrt{14.515 \times 245.0291}} = 0.97528 \quad (5)$$

Except for the above method, we can also adopt the EXCLE method to acquire r . We can utilize the CORREL function to exactly compute the correlation coefficients in Microsoft Office Excel, and the concrete program is

$$f_x = \text{CORREL}(A_1 : A_n, B_1 : B_m) \quad (6)$$

Where, A_1 is the first item of the independent variable sequence, A_n is the last item of the sequence, B_1 is the first item of the attributive variable sequence, and B_m is the last item of the corresponding sequence.

Using this method, we can obtain the correlation coefficient of the square taper transducer in Table 1, and the scatter diagram corresponding with this group of data is Figure 2.

Therefore, the scatter diagram of transducer transmission character and the correlation coefficient are two sorts of description of the linearization degree, and the scatter diagram is a sort of diagram method which can not be quantified. But the correlation coefficient is abstract and exact, and it can give exact answer to the difference between result and ideal objective. They describe the transmission characters of the transducer from two different aspects.

4. Transducer structure parameter adjustment and quantity transmission character improvement

From the capacitance transducer scatter diagram of above parallel flat structure, we can see that the linearization degree of the quantity transmission character corresponding with this group of data is not high, and the transducer must be improved from the structure, so how to improve the linearization degree through changing the structure of the transducer.

The design principle of most transducers is to confirm the value region range with measurement values between one

non-electric physical quantity x with another one electric physical quantity y first, and then design corresponding structure according to certain quantity transmission principle existing in these two physical quantities.

In the transducer technology, the linearization degree of the transducer will directly influence the later application of the transducer. The quality of the correlation is reflected by the correlation coefficient, i.e. the correlation coefficient of the transducer is more close to the maximum 1, its linearization degree is higher, and the design aim of the transducer should make its correlation coefficient approach 1 infinitely, thus the burden of the latter measurement circuit will be smaller and the measurement precision of the apparatus will be higher, or else, the transmission function with low linearization degree will increase the difficulty to the linearization processing work for the later measurement circuit, and directly influence the precision class of the measuring apparatus.

Through repetitive researches to the geometric structure of the transducer, we find that in the design of the transducer, the linearization degree of many transducers are always optimized by adjusting their geometric structure parameters, and the linearization degree can be denoted by the correlation coefficient r of the data list of the input and output, and for the ideal linear correlation character of the transmission function, the correlation coefficient should be 100%, i.e. $r=1$. In actual situation, the correlation coefficient is always little smaller than 1 because of various reasons. Obviously, 1 is the upper limit of the actual transducer correlation coefficient, and the difference with 1 is smaller, its linearization is higher. In general economic data statistics, if only the correlation coefficient among data sequences achieves above 0.8, it thinks high correlation is possessed among data sequences, but in the researches between the structure parameters of the transducer and its linear correlation coefficient, we must use the concept of engineering science to study the problem, and the judgment standards of the correlation are much higher, and for the transducer used in precision measuring apparatus, we divide the correlation coefficient r into three value regions and three corresponding classes, i.e. low correlation, significant correlation and high correlation (seen in Table 2).

Next, taking the capacitance solid particulate matter moisture transducer as the example, we introduce the application of the correlation coefficient method. The initial structure of the transducer is seen in Figure 3, and this is a sort of square taper double-pole capacitance transducer, and in the transmission function, the moisture content of the measured matter is the independent variable, and the electric capacitance of the transducer is the attributive variable. When designing the moisture tester of quartz sand, the moisture content and output capacitance values and the moisture content scatter diagram respectively are seen in x and y in Table 1 and Table 2. From the tables, we can see that though various scatter points of the moisture content and the output capacitance are not in one beeline, but it goes to linearization. Through analyzing the space distribution character of static filed of the square taper capacitance, because the electric field lines have serious aberrances in the marginal region of the pole board, which is the main reason to induce the non-linear transmission character. To improve the linear correlation character, we change the former square taper structure design to circular taper structure of the transducer electric pole board (seen in Figure 4). According to the Euler polygons digital method, we can acquire exact spatial electric field line distribution ((a) and (b) in Figure 4 reflect the fact that the aberrances of the electric field line distribution obvious weaken when the structure of the transducer is changed from square taper to circular taper). Then further increase the radius of the electric pole in the column, and basically control the marginal aberrance of the electric field in the ideal degree (seen in Figure 5 and Table 2).

In the above structure parameter adjustment process of the transducer and the corresponding electric field distribution, we can obviously see that the serious aberrance occurs in the marginal region of the electric field distribution of the square taper transducer parallel pole board, and after the interior and exterior electric poles are changed into cylinder structure and circular arc face structure, the aberrance in the marginal region of the electric filed distribution is obviously improved, and after the exterior electric pole doesn't change and the electric pole radius in the cylinder increase, we acquire ideal electric filed distribution.

The influence induced by the marginal aberrance can be ignored basically. Taking the quartz sand with even granularity as the measured matter, we respective use the capacitance transducers with above three different structures to measure the moisture, and the acquired data are seen in Table 4 and their corresponding scatter diagrams are respectively seen in Figure 6 and Figure 7. Comparing Figure 2 with Figure 6 and Figure 7, we can see that, every time adjustment of transducer structure parameters can improve the linearization degree, and the corresponding

correlation coefficient is more and more close to the maximum 1. Using the EXCEL-CORREL function method, we can compute the correlation coefficients of three groups of data as follows.

The first group (parallel flat structure): $r_1 = 0.97528$

The second group (small inner core structure): $r_2 = 0.990561$

The third group (big inner core structure): $r_3 = 0.997494$

5. Conclusions

Comparing the correlation coefficients of the transducers with three sorts of structure and corresponding scatter diagrams, we can see that the transducer linearization degree with the parallel flat structure belongs to the level of “low correlation”, and the transducer linearization degree with the small inner core structure belongs to the level of “significant correlation”, and the transducer linearization degree with the big inner core structure belongs to the level of “high correlation”, and obviously, the big inner core structure is a sort of ideal structure. Therefore, in the actual measuring works, for the granular solid matter, the square taper transducer has best acceptance nature to the measured matters (such as rapeseed and other croppers), and the second scheme after improvement takes second place, and the third scheme is the worst one, and the designer can carefully balance the advantages and disadvantages to the using object of the transducer.

Obviously, through analyzing the correlation coefficients of the transducer, we can make the structure parameters of the transducers continually approach to the ideal value of the correlation coefficient ($r = 1$), and finally make the quantity transmission character of the transducer achieve ideal level. This method can be generally used in the structure design of the transducer.

References

- Liu, Douren & Han, Baojun. (2003). *Transducer Principle and Application Technology*. Xi'an: Xi'an Electrical Science and Technology University Press. P.237-239.
- OMRON. (1999). *Transducer (Mini Edition)*. P.772-7512.
- Sang, Bingju. (1989). Transducer Transmission Character Curve Fitting. *Aero Weaponry Experiment Shooting Range*. No.2.
- Sun, Baowen & Yang, Baoqing. (2004). *Transducer and Application Manual*. Beijing: Mechanical Industry Press. P.223-244.
- Yang, Bangwen. (2004). *Practical Handbook of New Transducer*. Beijing: Renmin Post Press. P.166-273.

Table 1. Transducer data and standard deviation list

No.	x	y	$x - \bar{x}$	$(x - \bar{x})^2$	$y - \bar{y}$	$(y - \bar{y})^2$	$(x - \bar{x})(y - \bar{y})$	xy
1	1.58	4.10	-1.54	2.3716	-7.14	50.9796	10.9956	6.4780
2	1.77	5.06	-1.35	1.8225	-6.18	38.1924	8.3430	8.9562
3	1.92	7.01	-1.20	1.4400	-4.23	17.8929	5.0760	13.4592
4	2.20	7.52	-0.92	0.8464	-3.72	13.8384	3.4224	16.5440
5	2.44	9.31	-0.68	0.4624	-1.93	3.7249	1.3124	22.7164
6	2.74	11.50	-0.65	0.4225	0.26	0.0676	-0.1690	31.5100
7	3.02	11.50	-0.10	0.0100	0.26	0.0676	-0.0260	34.7300
8	3.37	11.85	0.25	0.0625	0.61	0.3721	0.1525	39.9345
9	3.71	12.73	0.59	0.3481	1.49	2.2201	0.8791	47.2283
10	4.02	13.51	0.90	0.8100	2.27	5.1529	2.0430	54.3102
11	4.29	17.50	1.17	0.3689	6.26	39.1876	7.3242	75.0750
12	4.64	16.82	1.52	2.3104	5.61	31.4721	8.5272	78.0448
13	4.92	17.71	1.80	3.2400	6.47	41.8609	11.6460	75.9759
Σ	40.62	146.12	-0.21	14.5153	0.03	245.0291	59.5264	504.9625

Note: $\bar{x} = 3.12, \bar{y} = 11.24$.

Table 2. Correlation class and correlation coefficient value region of capacitance transducer

Correlation class	Low correlation	Significant correlation	High correlation
r value region	0.980000~0.984000	0.986000~0.992000	0.994000~0.998000

Table 3. Parameter adjustment of capacitance transducer structure

Geometric structure	Structural parameters			
	$a(mm)$	$\phi(^{\circ})$	$R_1(mm)$	$R_2(mm)$
Before adjustment	86	40	6	46
After adjustment	120	45	11	46

Table 4. Moisture content and output capacitance correlation table obtained by square taper transducer when measuring quartz sand samples

Test No.	First group (parallel flat structure)		Second group (small inner core structure)		Third group (big inner core structure)	
	Moisture H (%)	Capacitance output Cx (pF)	Moisture H (%)	Capacitance output Cx (pF)	Moisture H (%)	Capacitance output Cx (pF)
01	1.58	4.10	1.60	4.09	1.57	3.79
02	1.77	5.06	1.79	5.02	1.72	5.01
03	1.92	7.01	1.92	5.94	1.97	6.22
04	2.20	7.52	2.20	6.97	2.24	7.54
05	2.44	9.31	2.43	8.56	2.43	9.00
06	2.74	11.50	2.74	11.2	2.77	10.67
07	3.02	11.50	3.06	12.07	3.11	12.01
08	3.37	11.85	3.39	12.09	3.46	13.02
09	3.71	12.73	3.70	14.31	3.71	14.37
10	4.02	13.51	4.06	14.99	4.06	15.96
11	4.29	17.50	4.36	17.32	4.32	17.30
12	4.64	16.82	4.67	17.33	4.63	18.62
13	4.92	17.71	4.90	18.95	4.92	19.51
Correlation coefficients	$r_1 = 0.97528$		$r_2 = 0.990561$		$r_3 = 0.997494$	

Note: Series sample moistures are prepared by the even soakage method.

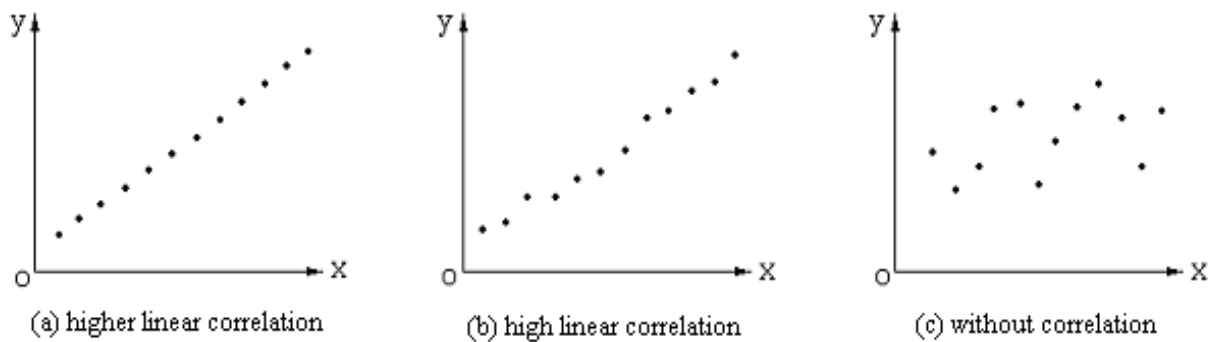


Figure 1. Scatter Diagram of Transducer Quantity Transmission Character

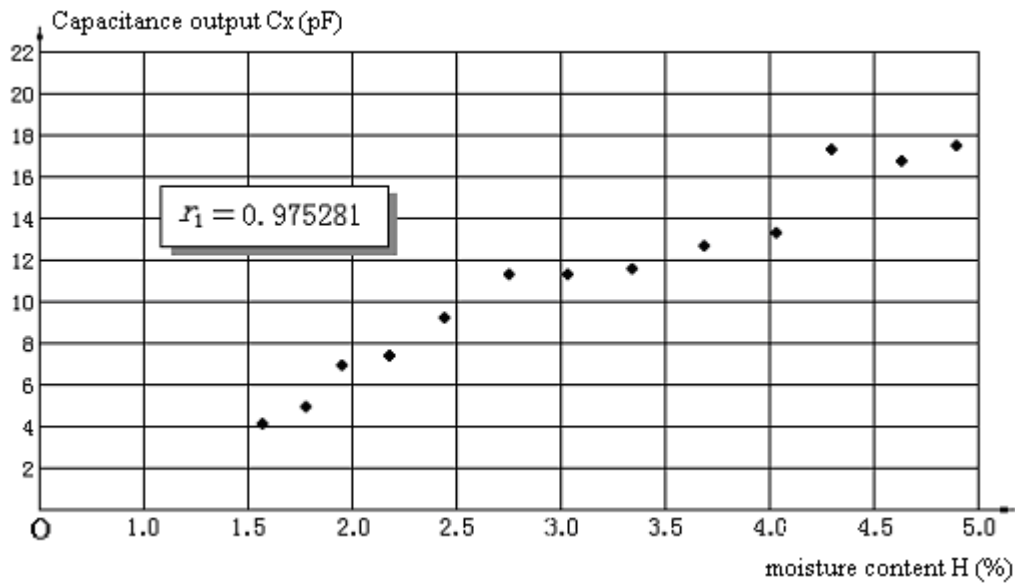


Figure 2. Scatter Diagram of the First Group (Parallel Flat Structural Transducer)

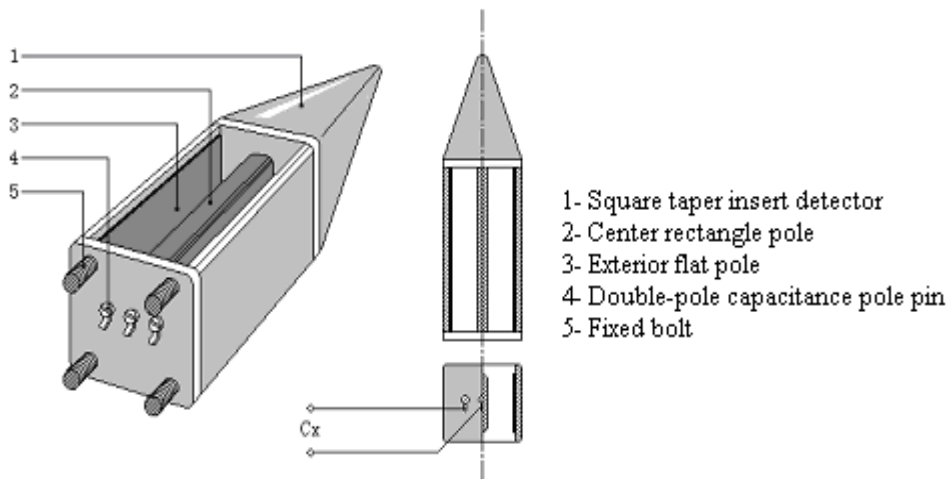


Figure 3. Square Taper Double-pole Capacitance Transducer Structure Sketch (Initial Stage Structure)

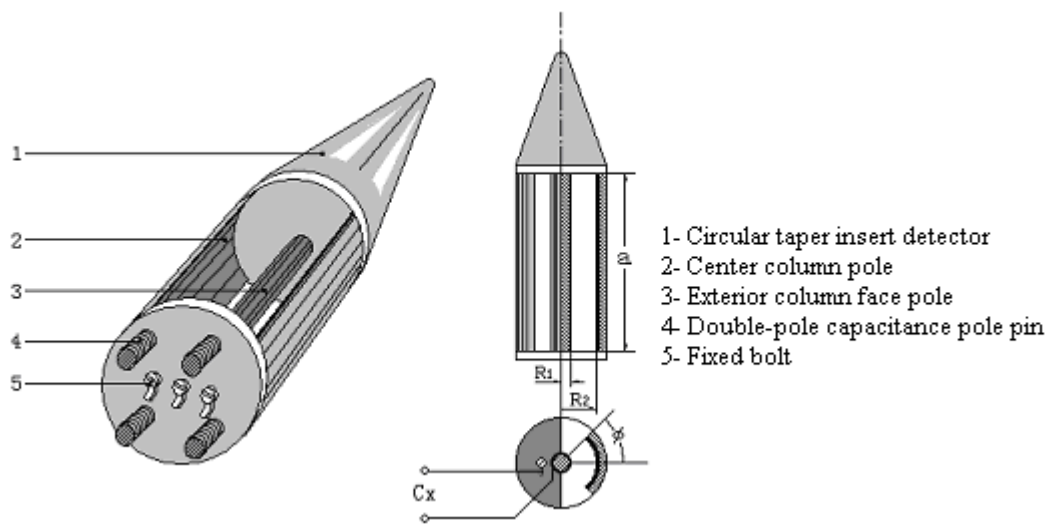


Figure 4. Circular Taper Double-pole Capacitance Transducer Structure Sketch (Improved)

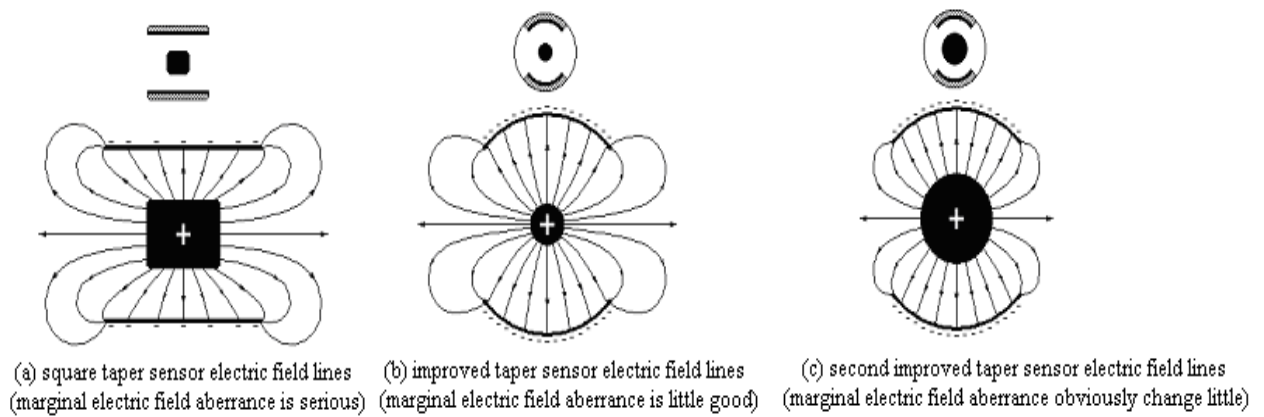


Figure 5. Different Transducer Structure and Electric Field Aberrance Degree

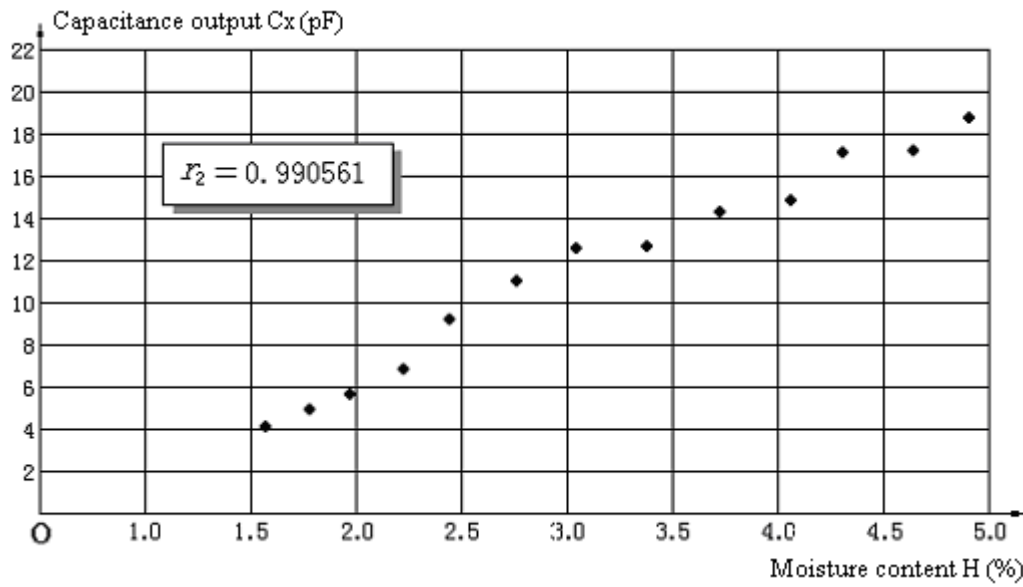


Figure 6. Scatter Diagram of the Second Group (Circular Taper Small Inner Core Capacitance Transducer Structure)

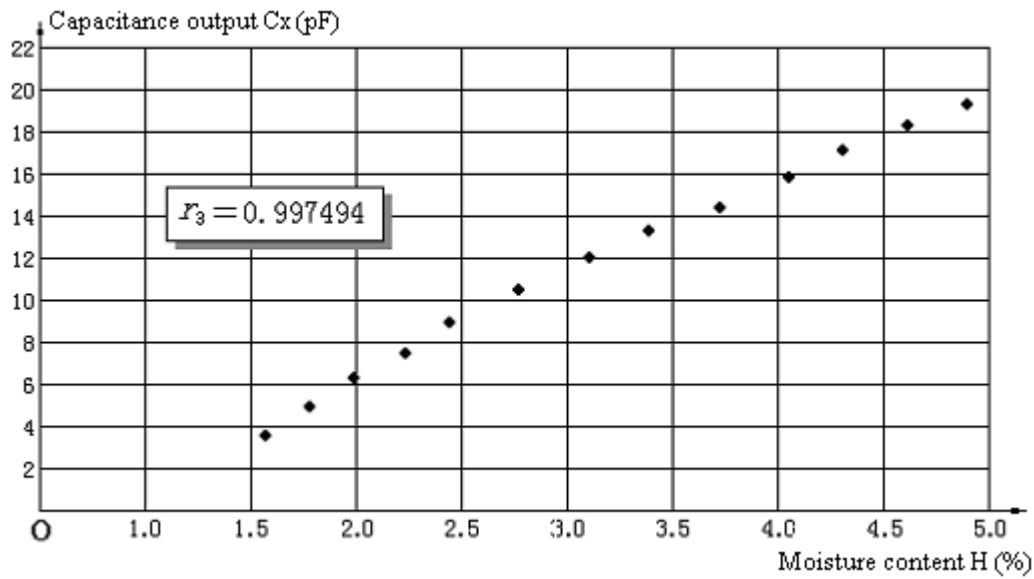


Figure 7. Scatter Diagram of the Third Group (Circular Taper Big Inner Core Capacitance Transducer Structure)



Effect of Nickel on the Structural Properties of Mn Zn Ferrite Nano Particles

C.Venkataraju (Corresponding author)

Department of Physics, A.M.A.College of Engineering

Vadamavandal, Near Kanchipuram, Tamilnadu

PIN 604 410, India

Tel: 91-4182-247-226 E-mail: cvraju_2k@yahoo.com

Abstract

Nano particles of $Mn_{0.5-x}Ni_xZn_{0.5}Fe_{2-x}O_4$ ($X = 0.0, 0.1, 0.2, 0.3$) have been synthesized by chemical co precipitation method. X-ray diffraction analysis confirms the formation of ferrites in nano phase. Lattice constant and particle size is found to be decreasing with increasing nickel concentration. The porosity calculated using x-ray density and measured density also shows a decreasing behavior with increasing nickel concentration.

Keywords: Ferrites, Chemical co-precipitation, Nanostructures, X-ray diffraction

1. Introduction

Manganese Zinc ferrite are technologically important materials because of their high magnetic permeability and low core loss. These ferrites have been extensively used in electronic applications such as transformers, choke coils, noise filters, recording heads etc. Ferrites prepared by conventional ceramic method involve high temperature which can result in the loss of their fine particle size. The bulk properties of the ferrites changes as one or more of its dimensions are reduced to nano size. (Y.Yamamoto, 1994; J.M.D Coey, 1972). The unusual properties exhibited by the ferrite nano particles and their promising technological applications have attracted much interest in recent years. The size and shape of the ferrite particles are dependent on the synthesis process. Wet chemical methods such as co-precipitation, sol gel and hydrothermal processing have been widely used to produce the fine particle size.

Bueno et al. (A.R.Bueno, 2007) have reported the influence of Manganese substitution on the magnetic properties and micro structure of $Ni_{0.5-x}Zn_{0.5-x}Mn_{2x}Fe_2O_4$ synthesized by nitrate-citrate precursor method. Verma et al (A.Verma, 2006) have reported the development of a new ferrite with low power loss based on Manganese Nickel Zinc Ferrite composition for switch mode power supplies. However few reports are available on the properties of nano Mn Ni Zn Ferrite. In the present investigation the studies on nano particles of $Mn_{0.5-x}Ni_xZnFe_2O_4$ ($x = 0.1, 0.2$ and 0.3) synthesized by chemical co-precipitation method is reported.

2. Experimental details

Nano particles of $Mn_{(0.5-x)}Ni_xZn_{0.5}Fe_2O_4$ with x varying from 0.0 to 0.3 were prepared by co-precipitation method. Aqueous solutions of $MnCl_2$, $ZnSO_4$, $NiCl_2$ and $FeCl_3$ in their respective stoichiometry (100 ml of solution containing $(0.5-x)$ M $MnCl_2$, (x) M $NiCl_2$, 0.5 M $ZnSO_4$ and 100 ml of 1M $FeCl_3$) were mixed thoroughly at $80^\circ C$ and this mixture was added to the boiling solution of NaOH (0.55 M dissolved in 1600 ml of distilled water) within 10 seconds under constant stirring and a pH of 11 was maintained throughout the reaction. Conversion of metal salts into hydroxides and subsequent transformation of metal hydroxide into nano ferrites takes place upon heating to $100^\circ C$ and maintained for 60 minutes. The nano particles thus formed were isolated by centrifugation and washed several

times with deionizer water followed by acetone and then dried at room temperature. The dried powder was grounded thoroughly in a clean agate mortar. The ground powder was then pelletized using hydraulic press and fired at 500 °C for 2 hrs. The structure and crystallite size were determined from the X-ray diffraction (XRD) measurements using Philips (PM 9220) diffract meter with CuK α ($\lambda = 1.5406 \text{ \AA}$) radiation.

3. Results and discussion

3.1 XRD analysis

The X-ray diffraction pattern for Mn_(0.5-x)Ni_xZn_{0.5}Fe₂O₄ (With x = 0.0, 0.1, 0.2, 0.3) is shown in the Fig (i). These diffraction lines provide clear evidence of the formation of ferrite phase in all the samples. The broad XRD line indicates that the ferrite particles are of nano size. The average particle size for each composition was calculated from the XRD line width of the (311) peak using Scherrer formula (Cullity B.D, 1966). The values of the particle size and lattice constant as deduced from the X-ray data are given in the Table 1.

The average particle size for Mn_{0.5}Zn_{0.5}Fe₂O₄ is found to be 13 nm and the particle size gradually decreases as the manganese concentration is decreased. This can be explained on the basis of cation stoichiometry. In a complex system like ferrites where many cations are involved, the nucleation and growth of the particles are expected to be influenced by the probability of a cation occupying available chemically inequivalent sites and its affinity to sites. For example, during the formation of MnFe₂O₄ nuclei, Mn²⁺ does not have strong preference of occupying only the tetrahedral site and a small fraction (<20%) can also occupy the octahedral site. In the nano scale range of the particles, Mn²⁺ gets uniformly distributed amongst the different sites with two octahedral sites and one tetrahedral site available to it. Therefore Mn²⁺ will have the highest probability of getting adsorbed by a growing nucleus (Chandana Rath, 2002). As the manganese concentration of the sample is replaced by nickel, the probability of Mn²⁺ getting adsorbed by a growing nucleus is low. This accounts for the decrease in particle size as the concentration of nickel is increased. The lattice constant decreases with increasing nickel concentration as shown in the Figure(2). This can be explained based on the relative ionic radius. The ionic radius (0.69Å) of Ni²⁺ ions is smaller than the ionic radius (0.82Å) of Mn²⁺ ions. Replacement of smaller Ni²⁺ cations for larger Mn²⁺ cations in the manganese zinc ferrite causes a decrease in lattice constant. However the lattice constant of the samples with nickel concentration up to x = 0.4 was found to be less than that of bulk. A significant fraction of Mn²⁺ and Zn²⁺ occupies the octahedral sites and forces Fe³⁺ to the tetrahedral sites against their chemical preferences. Since Fe³⁺ ions have smaller ionic radius (0.64Å), occupying the tetrahedral sites in place of larger divalent ions leads to contraction in lattice parameter as observed.

The measured density, ρ_m was determined using the formula

$$\rho_m = \frac{m}{\pi r^2 h}$$

Where m is the mass, r the radius and h the height of the sample.

The x-ray densities were calculated using the relation.

$$\rho_x = \frac{8m}{Na^3}$$

Where M is the molecular weight of the sample, N is the Avogadro's number and a is the lattice constant. The x-ray density (ρ_x) depends on the lattice constant and molecular weight of the sample, where as the measured density (ρ_m) of the samples is calculated from the geometry and mass of the samples. It is observed from the table 1 that the x-ray density increases with the increase of Ni concentration. Since the x-ray density is inversely proportional to the lattice constant, it increases as the lattice constant decreases. The measured density of the ferrite was found to be increasing with x . The porosity P of the ferrite nano particles was determined using the relation.

$$P = 1 - \frac{\text{bulkdensity}}{\text{x-raydensity}}$$

The variation in porosity with the nickel concentration for all the samples is shown in the Figure (3). It is found that the porosity decreases with increase in nickel concentration.

4. Conclusion

Nano structured Mn Ni Zn Ferrite was prepared by chemical co precipitation method. Structural analysis with XRD indicates the formation of Mn Ni Zn Ferrite. It is found that as the nickel concentration of the sample is increased, the lattice parameter and particle size decreases. Porosity, calculated using both densities, also shows a decrease trend with increasing nickel concentration.

References

- A.R.Bueno, Maria L.Gregori, Maria C.S, Nobrega, Mater.Chem.Phys, 105, (2007) p.229-233.
- A.Verma, M.I.Alam, Ratnamala Chatterjee, T.C.Goel, R.G.Mendiratta, J. Magn.Magn.Mater, 300 (2006) 500 – 505.
- Chandana Rath, S.Anand, R.P.Das, K.K.Sahoo, S.D.Kulkarni, S.K.Date and N.C.Mishra, J.Appl.Phys, 91 (2002) 2211.
- Cullity B.D, Elements of X-Ray Diffraction, Addison –Wesley Pub.Co. INC, (1966), 42.
- J.M.D Coey and K.Khalafella, Phys, Status Solidi, A11, (1972). 225.
- Y.Yamamoto and A.Makino, J.Magn.Magn.Mater, 133, (1994). 500.

Table 1. Lattice Constant, Particle size and Porosity of the prepared samples

x	Composition	Lattice Constant (Å)	Particle Size nm	Measured density (ρ_m)	X-ray density (ρ_x)	Porosity (%)
0.0	Mn _{0.5} Zn _{0.5} Fe ₂ O ₄	8.426	11.72	2.702	5.236	48.39
0.1	Mn _{0.4} Ni _{0.1} Zn _{0.5} Fe ₂ O ₄	8.410	11.16	2.887	5.272	45.23
0.2	Mn _{0.3} Ni _{0.2} Zn _{0.5} Fe ₂ O ₄	8.394	10.68	2.928	5.311	44.86
0.3	Mn _{0.2} Ni _{0.3} Zn _{0.5} Fe ₂ O ₄	8.378	10.02	3.275	5.350	38.77

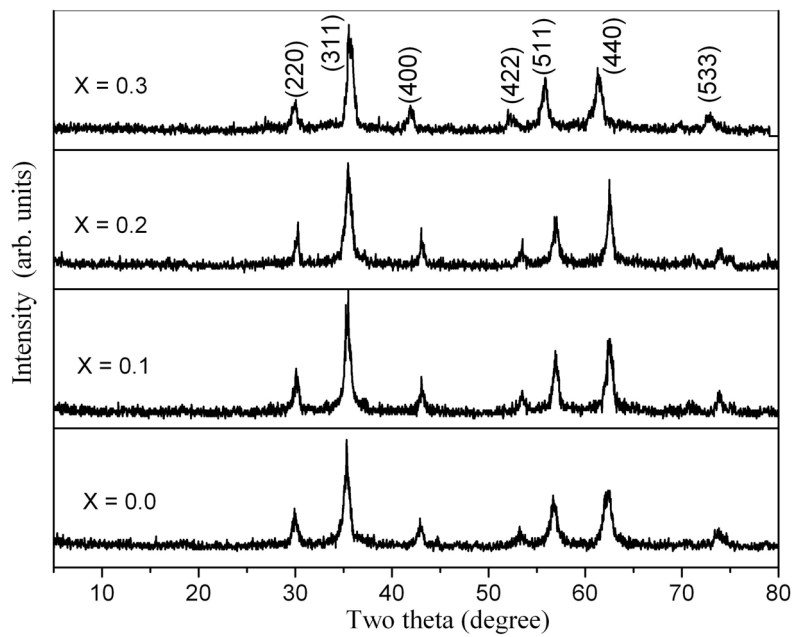


Figure 1. X-ray Diffraction pattern for the composition $\text{Mn}_{0.5-x}\text{Ni}_x\text{Zn}_{0.5}\text{Fe}_{2-x}\text{O}_4$ ($X = 0.0, 0.1, 0.2, 0.3$)

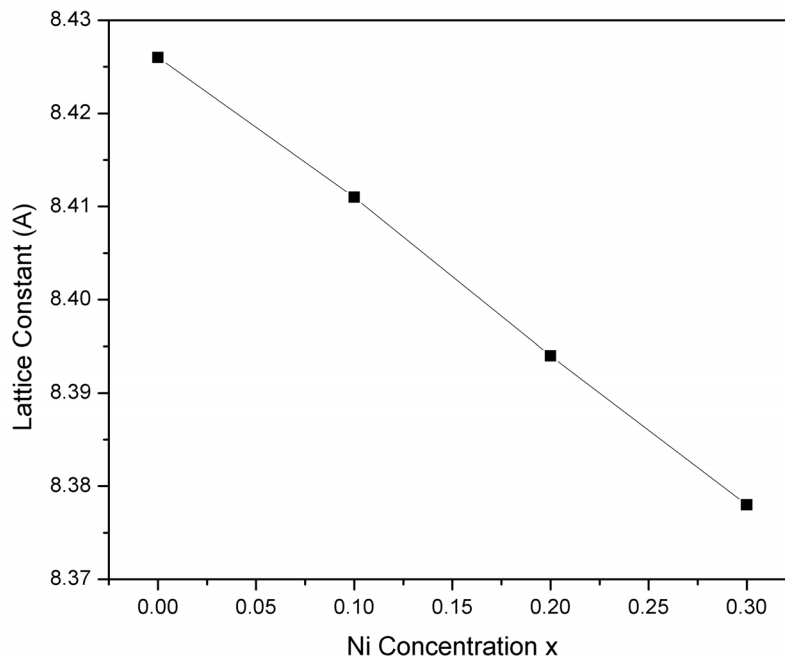


Figure 2. Lattice Constant (A) for the composition $\text{Mn}_{0.5-x}\text{Ni}_x\text{Zn}_{0.5}\text{Fe}_{2-x}\text{O}_4$ ($X = 0.0, 0.1, 0.2, 0.3$)

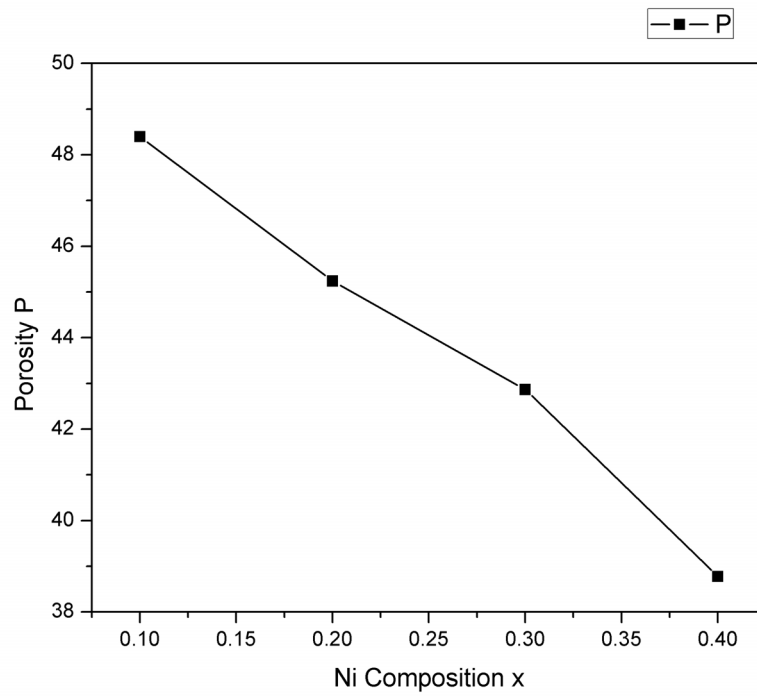


Figure 3. Porosity for the composition $\text{Mn}_{0.5-x}\text{Ni}_x\text{Zn}_{0.5}\text{Fe}_{2-x}\text{O}_4$ ($X = 0.0, 0.1, 0.2, 0.3$)



On the Independence of KVL

Zaiqi Fu & Wenliang Wu

Department of Physics, Zhaotong Teacher's College

Tel: 86-870-215-3826 E-mail: zhxfzq@126.com

Abstract

Analyze the limitations of several methods to select cycle circuit, put forward a method to select independent cycle circuit freely, namely, to judge with symmetrical difference.

Keywords: Kirchhoff's law, Independent cycle circuit, Symmetrical difference

1. Introduction

For the complicated linear circuit, we can set out current equation and voltage equation to find the solution according to Kirchhoff's Current Law (KCL) and Kirchhoff's Voltage Law (KVL). To a circuit with n knots and p branches, there are $n-1$ independent knot current equations, we can select any $n-1$ knots, and there are $m(m=p-n+1)$ independent circuits, to which we can set out m independent cycle circuit voltage equations, therefore, get p independent equations and work out the current values of all branches. However, errors often occur when choosing independent cycle circuits from many cycle circuits to set out independent voltage equations. The phenomenon is researched in lots of literature. The method to judge the independence of circuit according to principle of symmetrical difference is put forward in this thesis.

2. Limitations of several rules to select cycle circuits

To a specific complicated circuit with n knots and p branches, the number of its independent equations is definite, namely, $m=p-n+1$. As for how to select m independent cycle circuits to set out these m independent equations, references (Li, Kemin, 2007; Cheng, Shouzhu, 2005; Liang, Chanbin, 1980) summed up some rules, but all these rules have limitations, some even have defects. The defects of rules in references (Cheng, Shouzhu, 2005; Liang, Chanbin, 1980) have been analyzed in reference (Li, Kemin, 2007), so it will not be discussed in this thesis. Two methods to select cycle circuit are introduced in references (Li, Kemin, 2007), one is method of single-chain cycle circuit, which needs the knowledge of topology; the other is the method of plane net hole, for the plane network, we can select all the net hole and set out a KVL equation for every net hole, which will constitute a group of independent equation. But it only fits plane network. For the plane network, we can also select in this way, namely, begin with a net hole, make the cycle circuit include a new net hole in the old net hole every time, then get m independent equations. The second method which to select cycle circuit conform to this rule: "In the newly select circuits, at least there is a branch which never appeared in the select circuit." But the rule is only the sufficient, not the necessary condition to make the select cycle circuit independent, if rigidly adhere to the rule, you can not select enough cycle circuit in many cases.

For example, for the circuit in the Figure 1(components are omitted), firstly, select cycle circuit $ADBECEFA$, then select cycle circuit $DEFD$, the two cycle circuits include all the branches, henceforth, no matter how to select, new branch will not occur. But it still needs two equations to work out the current values of all branches.

The method of plane net hole does not fit three-dimensional network. The method of the single chain cycle circuit is

too complicated in use. In fact, to a complicated circuit, there are lots of selections to set out KVL equations, as long as the listed m equations are independent to one another. The method of plane net hole and single-chain cycle circuit set way to select independent cycle circuit in prescribed order, lacking flexibility. The following is a method to judge the independence of selected cycle circuits, which will improve the flexibility to select cycle circuit.

3. Set out KVL equations by judging with symmetrical difference

Symmetrical difference is a kind of operation of set, often indicated with “ Δ ”. The symmetrical difference of two sets (A and B) is defined as: $A \Delta B = A \cup B - A \cap B$ (Kuratowski, Kazimierz & Mostowski, Andraej, 1976), and the operation of symmetrical difference conforms to commutative law and associative law. The simple operation of the symmetrical difference of a number of sets is put forward in reference (Deng, Shude, 2000), namely, if an element belongs to odd number of sets of n sets, then the element will belong to the symmetrical difference set of these n sets; whereas, if an element belongs to even number of sets of these n sets, then the element will not belong to the symmetrical difference set (particularly, if an element doesn't belong to any set of these n sets, then it doesn't belong to the symmetrical difference set too). From reference (Deng, Shude, 2000), it's easy to find the character of the operation of symmetrical difference of sets, if the symmetrical difference of k sets is set C , then these k sets plus set C is $k+1$ sets, its symmetrical difference is empty set Φ , whereas, if the symmetrical difference of k sets is Φ , then the symmetrical difference of any $k-1$ sets of these k sets is the left set.

Firstly, number the branches, for example in Figure 1, indicate branch FAD with 1, DBE with 2, and so on, just like Figure 2. Cycle circuit represents a set which is composed of branches, such as the cycle circuit $DBED = \{2, 5\}$, the cycle circuit $ADBECEFA = \{1, 2, 3\}$ in Figure 1. We could demonstrate that any h cycle circuits are dependent when the symmetrical difference of the h sets representing h cycle circuits is Φ ; and any j ($2 \leq j \leq h$) cycle circuits which we select from h sets, if the symmetrical difference set of the j sets is not Φ , then the h cycle circuits are independent.

Therefore a method selecting independent cycle circuits is obtained.

For m independent cycle circuits, which is composed of p branches, each branch is given a number firstly, these numbers compose a set. Selecting any two cycle circuits, then the symmetrical difference of two cycle circuits (i.e. the symmetrical difference of two sets representing this two cycle circuits) is calculated. If the symmetrical difference set represents a cycle circuit, then the cycle circuit is dependent with the two cycle circuits, thus we can not select this cycle circuit yet.

Based on the previous principle, we select the third cycle circuit. It is calculated that the symmetrical difference of the third cycle circuit and every of previous two cycle circuits selected. And it is calculated that the symmetrical difference of the three cycle circuits too. Thus three symmetrical differences are obtained. If some sets or a set of the three symmetrical differences represent cycle circuits, then the cycle circuits are dependent with the three cycle circuits selected, thus we can not select this cycle circuits yet.

Then we select the fourth cycle circuit, and calculate the symmetrical differences of the fourth cycle circuit and every of previous three cycle circuits, the fourth cycle circuit and any two cycle circuits of previous three cycle circuits, and the four cycle circuits. Therefore the seven symmetrical differences are obtained, If some sets of the seven symmetrical differences represent cycle circuits, then the cycle circuits are dependent with the four cycle circuits selected, thus we can not select them yet.

Keep up to the m th cycle circuit. The m cycle circuits we select are independent each other, therefore m independent equations of KVL are obtained.

Such as $m=4, p=6$ in Figure 2, we select two cycle circuits $DBED = \{2, 5\}$ and $FDEF = \{4, 5, 6\}$ firstly, then calculate the symmetrical difference of two cycle circuits, we have

$$\{2, 5\} \Delta \{4, 5, 6\} = \{2, 4, 6\}.$$

$\{2, 4, 6\}$ represents the cycle circuit $BDFEB$. We can not select the cycle circuit $BDFEB$ later.

Second, we select the third cycle circuit, such as we select $CFEC = \{3, 6\}$. We have

$$\{2, 5\} \Delta \{3, 6\} = \{2, 3, 5, 6\}, \quad \{4, 5, 6\} \Delta \{3, 6\} = \{3, 4, 5\}$$

$$\{2, 5\} \triangleleft \{4,5,6\} \triangleleft \{3,6\} = \{2,3,4\}$$

In the three sets obtained, the set $\{3, 4, 5\}$ represents the cycle circuit $CFDEC$, and the set $\{2, 3, 4\}$ represents the cycle circuit $BDFCEB$. The fourth cycle circuit can not select $CFDEC$ and $BDFCEB$.

Finally, we select the fourth cycle circuit. Except $CFDEC$, $BDFCEB$ and $BDFEB$, any new cycle circuit can be selected. It is independent with previous three cycle circuits selected.

Obviously, Writing the KVL equations by symmetrical difference are not only flexibility, but also to judge the independence of cycle circuits

References

- Cheng, Shouzhu & Jiang Zhiyong. (2005). General Physics (2). 5th ed. Beijing: Higher Education Press, p180-180.
- Deng, Shude. (2000). The symmetric difference about sets. *Journal of Guyuan Teachers College* (Natural Science Edition), 21(6):p3-5.
- Kuratowski, Kazimierz & Mostowski, Andraej. (1976). *Set theory* (second). New York:PWMN, p7-18.
- Li, Kemin. (2007). Two kinds of right methods used in the course of choosing independent cycle circuit. *College Physics*, 26(2): p19-21.
- Liang, Chanbin & Qin, Guangrong. (1980). *Electromagnetics*. Beijing: Higher Education Press, 240-240.

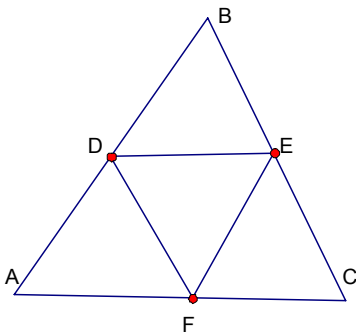


Figure 1.

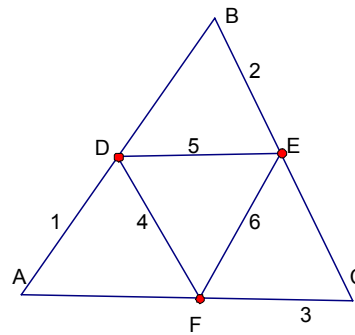


Figure 2.

A journal archived in Library and Archives Canada
A journal indexed in Canadiana (The National Bibliography)
A journal indexed in AMICUS
A journal indexed in Google Scholar
A journal indexed in Genamics JournalSeek

Applied Physics Research

Semiannual

Publisher Canadian Center of Science and Education
Address 4915 Bathurst St. Unit # 209-309, Toronto, ON. M2R 1X9
Telephone 1-416-208-4027
Fax 1-416-208-4028
E-mail apr@ccsenet.org
Website www.ccsenet.org
Printer William Printing Inc.
Price CAD.\$ 20.00

